

1 LEVERAGING MULTI-MESSENGER ASTROPHYSICS FOR DARK MATTER SEARCHES

By

Daniel Nicholas Salazar-Gallegos

A DISSERTATION

Submitted to  
Michigan State University  
in partial fulfillment of the requirements  
for the degree of

Physics—Doctor of Philosophy  
Computational Mathematics in Science and Engineering—Dual Major

Today

**ABSTRACT**

3 I did Dark Matter with HAWC and IceCube. I also used Graph Neural Networks

<sup>4</sup> Copyright by

<sup>5</sup> DANIEL NICHOLAS SALAZAR-GALLEGOS

<sup>6</sup> Today

## ACKNOWLEDGMENTS

8 I love my friends. Thanks to everyone that helped me figure this out. Amazing thanks to the people  
9 at LANL who supported me. Eames, etc Dinner Parties Jenny and her child Kaydince Kirsten, Pat,  
10 Andrea Family. You're so far but so critical to my formation. Unconditional love. Roommate

## TABLE OF CONTENTS

12	LIST OF TABLES . . . . .	vii
13	LIST OF FIGURES . . . . .	viii
14	LIST OF ABBREVIATIONS . . . . .	xiii
15	CHAPTER 1      INTRODUCTION . . . . .	1
16	CHAPTER 2      DARK MATTER IN THE COSMOS . . . . .	2
17	2.1 Introduction . . . . .	2
18	2.2 Dark Matter Basics . . . . .	3
19	2.3 Evidence for Dark Matter . . . . .	4
20	2.4 Searching for Dark Matter: Particle DM . . . . .	11
21	2.5 Sources for Indirect Dark Matter Searches . . . . .	16
22	2.6 Multi-Messenger Dark Matter . . . . .	18
23	CHAPTER 3      MULTIMESSENGER ASTROPHYSICS: DETECTING HIGH EN-	
24	ERGY NEUTRAL MESSENGERS . . . . .	21
25	3.1 Introduction . . . . .	21
26	3.2 Charged Particles in a Medium . . . . .	21
27	3.3 Photons ( $\gamma$ ) . . . . .	22
28	3.4 Neutrinos ( $\nu$ ) . . . . .	22
29	3.5 Opportunities to Combine for Dark Matter . . . . .	22
30	CHAPTER 4      HIGH ALTITUDE WATER CHERENKOV (HAWC) OBSERVATORY .	24
31	4.1 The Detector . . . . .	24
32	4.2 Events Reconstruction and Data Acquisition . . . . .	24
33	4.3 Remote Monitoring . . . . .	24
34	CHAPTER 5      ICECUBE NEUTRINO OBSERVATORY . . . . .	25
35	5.1 The Detector . . . . .	25
36	5.2 Events Reconstruction and Data Acquisition . . . . .	25
37	5.3 Northern Test Site . . . . .	25
38	CHAPTER 6      COMPUTATIONAL TECHNIQUES IN PARTICLE ASTROPHYSICS .	26
39	6.1 Neural Networks for Gamma/Hadron Separation . . . . .	26
40	6.2 Parallel Computing for Dark Matter Analyses . . . . .	26
41	CHAPTER 7      GLORY DUCK: MULTI-WAVELENGTH SEARCH FOR DARK MATT-	
42	TER ANNIHILATION TOWARDS DWARF SPHEROIDAL GALAX-	
43	IES . . . . .	27
44	7.1 Introduction . . . . .	27
45	7.2 Dataset and Background . . . . .	29
46	7.3 Analysis . . . . .	31

47	7.4 HAWC Results . . . . .	38
48	7.5 Glory Duck Combined Results . . . . .	39
49	7.6 HAWC Systematics . . . . .	43
50	7.7 <i>J</i> -factor distributions . . . . .	48
51	7.8 Discussion and Conclusions . . . . .	53
52	<b>CHAPTER 8 NU DUCK . . . . .</b>	<b>57</b>
53	<b>CHAPTER 9 MULTITHREADING HAWC ANALYSES FOR DARK MATTER</b>	
54	<b>SEARCHES . . . . .</b>	<b>58</b>
55	<b>APPENDIX FIRST APPENDIX . . . . .</b>	<b>59</b>
56	<b>BIBLIOGRAPHY . . . . .</b>	<b>60</b>

## LIST OF TABLES

<p>58    Table 7.1    Summary of the relevant properties of the dSphs used in the present work.      59    Column 1 lists the dSphs. Columns 2 and 3 present their heliocentric distance      60    and galactic coordinates, respectively. Columns 4 and 5 report the <math>J</math>-factors of      61    each source given from the <math>\mathcal{GS}</math> and <math>\mathcal{B}</math> independent studies and their estimated      62    <math>\pm 1\sigma</math> uncertainties. The values <math>\log_{10} J</math> (<math>\mathcal{GS}</math> set) [44] correspond to the mean      63    <math>J</math>-factor values for a source extension truncated at the outermost observed star.      64    The values <math>\log_{10} J</math> (<math>\mathcal{B}</math> set) [46] are provided for a source extension at the tidal      65    radius of each dSph. <b>Bolded sources are within HAWC's field of view and</b>      66    <b>provided to the Glory Duck analysis.</b></p>	<p style="margin-top: 100px;">. . . . . 35</p>
<p>67    Table 7.2    Summary of dSph observations by each experiment used in this work. A      68    ‘-’ indicates the experiment did not observe the dSph for this study. For      69    Fermi-LAT, the exposure at 1 GeV is given. For HAWC, <math> \Delta\theta </math> is the absolute      70    difference between the source declination and HAWC latitude. HAWC is more      71    sensitive to sources with smaller <math> \Delta\theta </math>. For IACTs, we show the zenith angle      72    range, the total exposure, the energy range, the angular radius <math>\theta</math> of the signal or      73    ON region, the ratio of exposures between the background-control (OFF) and      74    signal (ON) regions (<math>\tau</math>), and the significance of gamma-ray excess in standard      75    deviations, <math>\sigma</math>.</p>	<p style="margin-top: 100px;">. . . . . 36</p>
<p>76    Proof I know how to include</p>	

## LIST OF FIGURES

78	Figure 2.1	Rotation curve fit to NGC 6503 from [7]. Dashed line is the contribution 79 from visible matter. Dotted curves are from gas. Dash-dot curves are from 80 dark matter (DM). Solid line is the composite contribution from all matter 81 and DM sources. Data are indicated with bold dots with error bars. Data 82 agree strongly with a matter + DM composite prediction. . . . .	5
83	Figure 2.2	Light from distant galaxy is bent in unique ways depending on the distribution 84 of mass between the galaxy and Earth. Yellow dashed lines indicate where 85 the light would have gone if the matter were not present [8]. . . . .	7
86	Figure 2.3	(left) Optical image of galactic cluster 1E0657-558. (right) X-ray image of the 87 cluster with redder meaning hotter and higher baryon density. (both) Green 88 contours are reconstruction of gravity contours from weak lensing. White 89 rings are the best fit mass maxima at 68.3%, 95.5%, and 99.7% confidence. 90 The matter maxima of the clusters are clearly separated from x-ray maxima. [9]	8
91	Figure 2.4	Plank CMB sky. Sky map features small variations in temperature in primor- 92 dial light. These anisotropies are used to make inferences about the universe's 93 energy budget and developmental history. [10] . . . . .	9
94	Figure 2.5	Observed Cosmic Microwave Background power spectrum as a function of 95 multipole moment from Plank [10]. Blue line is best fit model from $\Lambda$ CDM. 96 Red points and lines are data and error, respectively. . . . .	10
97	Figure 2.6	Predicted power spectra of CMB for different $\Omega_m h^2$ values for fixed baryon 98 density from [11]. (left) Low $\Omega_m h^2$ increases the prominence of first and 99 second peaks. (middle) $\Omega_m h^2$ is most similar to the observed power spectrum. 100 The second and third peaks are similar in height. (right) $\Omega_m h^2$ is large which 101 suppresses the first peak and raises the prominence of the third peak. . . . .	10
102	Figure 2.7	The Standard Model (SM) of particle physics. Figure taken from <a href="http://www.quantumdiaries.org/2014/03/14/the-standard-model-a-beautiful-but-flawed-theory/">http://www.quantumdiaries.org/2014/03/14/the-standard-model-a-beautiful-but-flawed-theory/</a> . . . . .	12
105	Figure 2.8	Simplified Feynman diagram demonstrating with different ways DM can 106 interact with SM particles. The 'X's refer to the DM particles whereas the 107 SM refer to fundamental particles in the SM. The large circle in the center 108 indicates the vertex of interaction and is purposely left vague. The colored 109 arrows refer to different directions of time as well as their respective labels. 110 The arrows indicate the initial and final state of the DM -SM interaction in time.	13

111	Figure 2.9 A single jet event in ATLAS detector from 2017 [16]. Jet momentum was 112 observed to be 1.9 TeV. Missing transverse momentum was observed to be 113 1.9 TeV compared to the initial transverse momentum of the event was 0. 114 Implied MET is traced by a red dashed line in event display. . . . .	14
115	Figure 2.10 More detailed pseudo-Feynman diagram of particle cascade from dark matter 116 annihilation into 2 quarks. The quarks hadronize and down to stable particles 117 like $\gamma$ or the anti-proton ( $p^-$ ). Diagram pulled from ICRC 2021 presentation 118 on DM annihilation search [17]. . . . .	15
119	Figure 2.11 Dark Matter (DM) decay spectrum for $b\bar{b}$ initial state and $\gamma$ final state. Redder 120 spectra are for larger DM masses. Bluer spectra are light DM masses. $x$ is a 121 unitless factor defined as the ratio of the mass of DM, $m_\chi$ , and the final state 122 particle energy $E_\gamma$ . Figure from [19]. . . . .	17
123	Figure 2.12 Different dark matter density profiles compared. Some models produce ex- 124 ceptionally large densities at small r [20]. . . . .	18
125	Figure 2.13 The Milky Way Galaxy in photons ( $\gamma$ ) and neutrinos ( $\nu$ ) [22]. The Galactic 126 center is at $l=0^\circ$ and is the brightest region in all panels. (top) An Optical 127 color image of the Milky Way galaxy seen from Earth. Clouds of gas and dust 128 obscure some light from stars. (2nd down) Integrated flux of $\gamma$ -rays observed 129 by the Fermi-LAT telescope [23]. (middle) Expected neutrino emission 130 that corresponds with Fermi-LAT observations. (2nd up) Expected neutrino 131 emission profile after considering detector systematics of IceCube. (bottom) 132 Observed neutrino emission from region of the galactic plane. Substantial 133 neutrino emission was detected. . . . .	19
134	Figure 2.14 Dark Matter annihilation spectra for different final state particle and standard 135 model annihilation channels [24]. Photons (red), $e^\pm$ (green), $\bar{p}$ (blue), $\nu$ (black). . . . .	20
136	Figure 3.1 TODO: Show a nuclear reactor with cherenkov radiation[NEEDS A SOURCE][FACT 137 CHECK THIS] . . . . .	22
138	Figure 3.2 TODO: absorption spectrum of liquid and solid water[NEEDS A SOURCE][FACT 139 CHECK THIS] . . . . .	23

140	Figure 7.1 [NEEDS A SOURCE] Sensitivities of five gamma-ray experiments compared 141 to percentages of the Crab nebula's emission and dark matter annihilation. 142 Solid lines present estimated sensitivities to power law spectra [FACT CHECK 143 THIS]for each experiment. Green lines are Fermi-LAT sensitivities where 144 lighter green is the sensitivity to the galactic center and dark green is its 145 sensitivity to higher declinations. Orange, red, and purple solid lines rep- 146 represent the MAGIC, HESS, and VERITAS 50 hour sensitivities respectively. 147 The maroon and brown lines are the HAWC 1 year and 5 year sensitivities. 148 Across four decades of gamma-ray energy, these experiments have similar 149 sensitivities on the order $10^{-12}$ erg cm $^{-2}$ s $^{-1}$ . The dotted lines are estimated 150 dark matter fluxes assuming $m_\chi = 5$ TeV DM annihilating to bottom quarks 151 (red), tau leptons (blue), and W bosons (green). Faded gray lines outline 152 percentage flux of the Crab nebula. . . . .	27
153	Figure 7.2 Effect of Electro-Weak (EW) corrections on expected DM annihilation spec- 154 trum for $\chi\chi \rightarrow W^-W^+$ . Solid lines are spectral models that consider EW 155 corrections. Dash-dot lines are spectral models without EW corrections. Red 156 lines are models for $M_\chi = 1$ TeV. Blue lines represent models for $M_\chi = 100$ 157 TeV. All models are sourced from the PPPC4DMID [43]. . . . .	32
158	Figure 7.3 $\frac{dJ}{d\Omega}$ maps for Segue1 (top) and Coma Berenices (bottom). Origin is centered 159 on the specific dwarf spheroidal galaxies (dSph). X and Y axes are the 160 angular separation from the center of the dwarf. Plots of the remaining 11 161 dSph HAWC studied are linked in TODO: cref to appendix. . . . .	34
162	Figure 7.4 Illustration of the combination technique showing a comparison between 163 $-2 \ln \lambda$ provided by four instruments (colored lines) from the observation 164 of the same dSph without any $J$ nuisance and their sum, <i>i.e.</i> the result- 165 ing combined likelihood (thin black line). According to the test statistics 166 of Equation (7.10), the intersection of the likelihood profiles with the line 167 $-2 \ln \lambda = 2.71$ indicates the 95% C.L. upper limit on $\langle \sigma v \rangle$ . The combined 168 likelihood (thin black line) shows a smaller value of upper limit on $\langle \sigma v \rangle$ 169 than those derived by individual instruments. We also show the uncertainties 170 on the $J$ -factor affects the combined likelihood and degrade the upper limit 171 on $\langle \sigma v \rangle$ (thick black line). All likelihood profiles are normalized so that the 172 global minimum $\widehat{\langle \sigma v \rangle}$ is 0. We note that each profile depends on the observa- 173 tional conditions in which a target object was observed. The sensitivity of a 174 given instrument can be degraded and the upper limits less constraining if the 175 observations are performed in non optimal conditions such as a high zenith 176 angle or a short exposure time. . . . .	39
177	Figure 7.5 HAWC upper limits at 95% confidence level on $\langle \sigma v \rangle$ versus DM mass for 178 seven annihilation channels, using the set of $J$ -factors from Ref. [47] The 179 solid line represents the observed combined limit. Dashed lines represent 180 limits from individual dSphs. . . . .	40

181	Figure 7.6 HAWC Brazil bands at 95% confidence level on $\langle\sigma v\rangle$ versus DM mass for	41
182	seven annihilation channels with $J$ -factors from $\mathcal{GS}$ [47]. The solid line	
183	represents the combined limit from 13 dSphs. The dashed line is the expected	
184	limit. The green band is the 68% containment. The yellow band is the 95%	
185	containment. . . . .	
186	Figure 7.7 Upper limits at 95% confidence level on $\langle\sigma v\rangle$ in function of the DM mass for	44
187	eight annihilation channels, using the set of $J$ factors from Ref. [47] ( $\mathcal{GS}$ set	
188	in Table 7.1). The black solid line represents the observed combined limit,	
189	the black dashed line is the median of the null hypothesis corresponding	
190	to the expected limit, while the green and yellow bands show the 68% and	
191	95% containment bands. Combined upper limits for each individual detector	
192	are also indicated as solid, colored lines. The value of the thermal relic	
193	cross-section in function of the DM mass is given as the red dotted-dashed	
194	line [52]. . . . .	
195	Figure 7.8 Same as Fig. 7.7, using the set of $J$ factors from Ref. [46, 51] ( $\mathcal{B}$ set in Table 7.1). . . . .	45
196	Figure 7.9 Comparisons of the combined limits at 95% confidence level for each of the	46
197	eight annihilation channels when using the $J$ factors from Ref. [47] ( $\mathcal{GS}$ set in	
198	Table 7.1), plain lines, and the $J$ factor from Ref. [46, 51] ( $\mathcal{B}$ set in Table 7.1),	
199	dashed lines. The cross-section given by the thermal relic is also indicated [52]. . . . .	
200	Figure 7.10 Comparisons of the combined limits at 95% confidence level for a point source	47
201	analysis and extended source using [47] $\mathcal{GS}$ J-factor distributions and PPPC	
202	[43] annihilation spectra. Shown are the limits for Segue1 which will have	
203	the most significant impact on the combined limit. 6 of the 7 DM annihilation	
204	channels are shown. Solid lines are extended source studies. Dashed lines	
205	are point source studies. Overall, the extended source analysis improves the	
206	limit by a factor of 2. . . . .	
207	Figure 7.11 Same as Fig. 7.10 on Coma Berenices. This dSph also contributes signifi-	48
208	cantly to the limit. The limits are identical in this case. . . . .	
209	Figure 7.12 Comparison of combined limits when correcting for HAWC's pointing sys-	49
210	tematic. All DM annihilation channels are shown. The solid black line is the	
211	ratio between published limit to the declination corrected limit. The blue solid	
212	line or "Combined_og" represented the limits computed for Glory Duck. The	
213	solid orange line or "Combined_ad" represented the limits computed after	
214	correcting for the pointing systematic. . . . .	
215	Figure 7.13 Differential map of $dJ/\Omega$ from model built in Section 7.7.1 and profiles	51
216	provided directly from authors. (Top) Differential from Segue1. (bottom)	
217	Differential from Coma Berenices. Note that their scales are not the same.	
218	Segue1 shows the deepest discrepancies which is congruent with its large	
219	uncertainties. Both models show anuli where unique models become apparent. . . . .	

220	Figure 7.14 HAWC limits for Coma Berenices (top) and Segue1 (bottom) for two different 221 map sets. Blue lines are limits calculated on maps with poor model repre- 222 sentation. Orange lines are limits calculated on spatial profiles provided by 223 the authors of [44]. Black line is the ratio of the poor spatial model limits to 224 the corrected spatial models. The left y-axis measures $\langle \sigma v \rangle$ for the blue and 225 orange lines. The right y-axis measures the ratio and is unitless. . . . .	52
226	Figure 7.15 Comparisons between the $J$ -factors versus the angular radius for the com- 227 putation of $J$ factors from Ref. [47] ( $\mathcal{GS}$ set in Table 7.1) in blue and for 228 the computation from Ref. [46, 51] ( $\mathcal{B}$ set in Tab. 7.1) in orange. The solid 229 lines represent the central value of the $J$ -factors while the shaded regions 230 correspond to the $1\sigma$ standard deviation. . . . .	54
231	Figure 7.16 Comparisons between the $J$ -factors versus the angular radius for the computa- 232 tion of $J$ factors from Ref. [47] ( $\mathcal{GS}$ set in Tab. 7.1) in blue and for the 233 computation from Ref. [46, 51] ( $\mathcal{B}$ set in Tab. 7.1) in orange. The solid 234 lines represent the central value of the $J$ -factors while the shaded regions 235 correspond to the $1\sigma$ standard deviation. . . . .	55

**LIST OF ABBREVIATIONS**

- 237 **MSU** Michigan State University  
238 **LANL** Los Alamos National Laboratory  
239 **DM** Dark Matter  
240 **SM** Standard Model  
241 **HAWC** High Altitude Water Cherenkov Observatory

242

## **CHAPTER 1**

### **INTRODUCTION**

243 Is the text not rendering right? Ah ok it knows im basically drafting the doc still

## CHAPTER 2

244

### DARK MATTER IN THE COSMOS

#### 245 2.1 Introduction

246 The dark matter problem can be summarized in part by the following thought experiment.

247 Let us say you are the teacher for an elementary school classroom. You take them on a field  
248 trip to your local science museum and among the exhibits is one for mass and weight. The exhibit  
249 has a gigantic scale, and you come up with a fun problem for your class.

250 You ask your class, "What is the total weight of the classroom? Give your best estimation to  
251 me in 30 minutes, and then we'll check your guess on the scale. If your guess is within 10% of the  
252 right answer, we will stop for ice cream on the way back."

253 The students are ecstatic to hear this, and they get to work. The solution is some variation of  
254 the following strategy. The students should give each other their weight or best guess if they do  
255 not know. Then, all they must do is add each student's weight and get a grand total for the class.

256 The measurement on the giant scale should show the true weight of the class. When comparing  
257 the measured weight to your estimation, multiply the measurement by  $1.0 \pm 0.1$  to get the  $\pm 10\%$   
258 tolerances for your estimation.

259 Two of your students, Sandra and Mario, return to you with a solution.

260 They say, "We weren't sure of everyone's weight. We used 65 lbs. for the people we didn't  
261 know and added everyone who does know. There are 30 of us, and we got 2,000 lbs.! That's a ton!"

262 You estimated 1,900 lbs. assuming the average weight of a student in your class was 60 lbs.  
263 So, you are pleased with Sandra's and Mario's answer. You instruct your students to all gather on  
264 the giant scale and read off the weight together. To all your surprise, the scale reads *10,000 lbs.*!  
265 10,000 is significantly more than a 10% error from 2,000. In fact, it is approximately 5 times more  
266 massive than either your or your students' estimates. You think to yourself and conclude there  
267 must be something wrong with the scale. You ask an employee to check the scale and verify it is  
268 well calibrated. They confirm that the scale is in working order. You weigh a couple of students  
269 individually to assess that the scale is well calibrated. Sandra weighs 59 lbs., and Mario weighs

270 62 lbs., typical weights for their age. You then weigh each student individually and see that their  
271 weights individually do not deviate greatly from 60 lbs. So, where does all the extra weight come  
272 from?

273 This thought experiment serves as an analogy to the Dark Matter problem. The important  
274 substitution to make however is to replace the students with stars and the classroom with a galaxy,  
275 say the Milky Way. Individually the mass of stars is well measured and defined with the Sun as our  
276 nearest test case. However, when we set out to measure the mass of a collection of stars as large as  
277 galaxies, our well-motivated estimation is wildly incorrect. There simply is no way to account for  
278 this discrepancy except without some unseen, or dark, contribution to mass and matter in galaxies.  
279 I set out in my thesis to narrow the possibilities of what this Dark Matter could be.

280 This chapter is organized like the following... **TODO: Text should look like ... Chapter x has**  
281 **blah blah blah.**

282 **2.2 Dark Matter Basics**

283 Presently, a more compelling theory of cosmology that includes Dark Matter (DM) in order  
284 to explain a variety of observations is  $\Lambda$  Cold Dark Matter, or  $\Lambda$ CDM. I present the evidence  
285 supporting  $\Lambda$ CDM in Section 2.3 yet discuss the conclusions of the  $\Lambda$ CDM model here. According  
286 to  $\Lambda$ CDM fit to observations on the Cosmic Microwave Background (CMB), DM is 26.8% of the  
287 universe's current energy budget. Baryonic matter, stuff like atoms, gas, and stars, contributes to  
288 4.9% of the universe's current energy budget [1, 2, 3].

289 DM is dark; it does not interact readily with light at any wavelength. DM also does not interact  
290 noticeably with the other standard model forces (Strong and Weak) at a rate that is readily observed  
291 [3]. DM is cold, which is to say that the average velocity of DM is below relativistic speeds [1].  
292 'Hot' DM would not likely manifest the dense structures we observe like galaxies, and instead  
293 would produce much more diffuse galaxies than what is observed [3, 1]. DM is old; it played a  
294 critical role in the formation of the universe and the structures within it [1, 2].

295 Observations of DM have so far been only gravitational. The parameter space available to what  
296 DM could be therefore is extremely broad. The broad DM parameter space is iteratively tested in

297 DM searches by supposing a hypothesis that has not yet been ruled out and performing observations  
298 to test them. When the observations yield a null result, the parameter space is constrained further.  
299 I present some approaches for DM searches in Section 2.4.

300 **2.3 Evidence for Dark Matter**

301 Dark Matter (DM) has been a looming problem in physics for almost 100 years. Anomalies  
302 have been observed by astrophysicists in galactic dynamics as early as 1933 when Fritz Zwicky  
303 noticed unusually large velocity dispersion in the Coma cluster. Zwicky's measurement was the  
304 first recorded to use the Virial theorem to measure the mass fraction of visible and invisible matter  
305 in celestial bodies [4]. From Zwicky in [5], "*If this would be confirmed, we would get the surprising*  
306 *result that dark matter is present in much greater amount than luminous matter.*" Zwicky's and  
307 others' observation did not instigate a crisis in astrophysics because the measurements did not  
308 entirely conflict with their understanding of galaxies [4]. In 1978, Rubin, Ford, and Norbert  
309 measured rotation curves for ten spiral galaxies [6]. Rubin et al.'s 1978 publication presented a  
310 major challenge to the conventional understanding of galaxies that could no longer be dismissed by  
311 measurement uncertainties. Evidence has been mounting ever since for this exotic form of matter.  
312 The following subsections provide three compelling pieces of evidence in support of the existence  
313 of DM.

314 **2.3.1 First Clues: Stellar Velocities**

315 Zwicky, and later Rubin, measured the stellar velocities of various galaxies to estimate their  
316 virial mass. The Virial Theorem upon which these observations are interpreted is written as

$$2T + V = 0. \quad (2.1)$$

317 Where  $T$  is the kinetic energy and  $V$  is the potential energy in a self-gravitating system. The  
318 classical Newton's law of gravity from stars and gas was used for gravitational potential modeled in  
319 the observed galaxies:

$$V = -\frac{1}{2} \sum_i \sum_{j \neq i} \frac{m_i m_j}{r_{ij}}. \quad (2.2)$$

320 Zwicky et al. measured just the velocities of stars apparent in optical wavelengths [5]. Rubin et al.  
 321 added by measuring the velocity of the hydrogen gas via the 21 cm emission line of Hydrogen [6].  
 322 The velocities of the stars and gas are used to infer the total mass of galaxies and galaxy clusters  
 323 via Equation (2.1). An inferred mass is obtained from the luminosity of the selected sources. The  
 324 two inferences are compared to each other as a luminosity to mass ratio which typically yielded [1]

$$\frac{M}{L} \sim 400 \frac{M_{\odot}}{L_{\odot}} \quad (2.3)$$

325  $M_{\odot}$  and  $L_{\odot}$  referring to stellar mass and stellar luminosity, respectively. These ratios clearly indicate  
 326 a discrepancy in apparent light and mass from stars and gas and their velocities.

327 Rubin et al. [6] demonstrated that the discrepancy was unlikely to be an underestimation of  
 328 the mass of the stars and gas. The inferred "dark" mass was up to 5 times more than the luminous  
 329 mass. This dark mass also needed to extend well beyond the extent of the luminous matter.

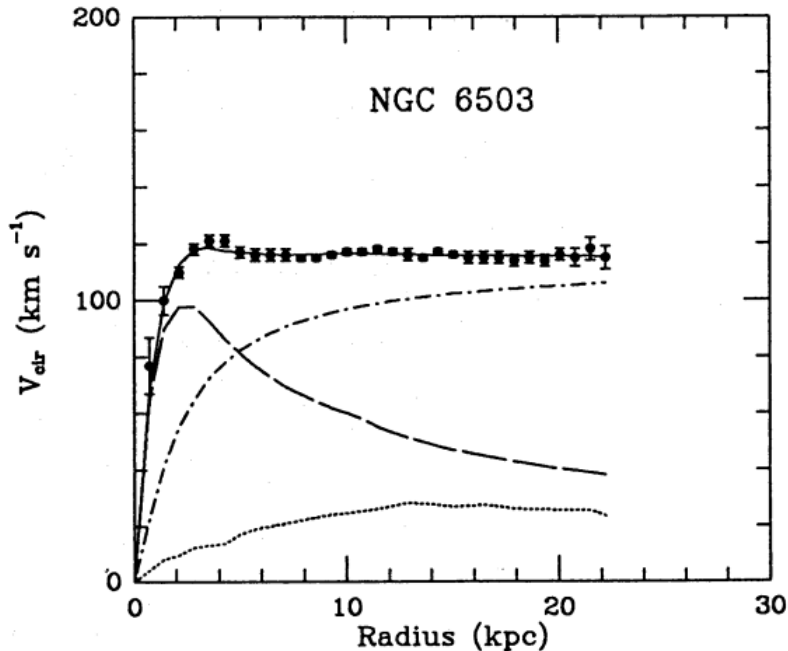


Figure 2.1 Rotation curve fit to NGC 6503 from [7]. Dashed line is the contribution from visible matter. Dotted curves are from gas. Dash-dot curves are from dark matter (DM). Solid line is the composite contribution from all matter and DM sources. Data are indicated with bold dots with error bars. Data agree strongly with a matter + DM composite prediction.

330 Figure 2.1 features one of many rotation curves plotted from the stellar velocities within galaxies.

331 The measured rotation curves mostly feature a flattening of velocities at higher radius which is not  
332 expected if the gravity was only coming from gas and luminous matter. The extension of the  
333 flat velocity region also indicates that the DM is distributed far from the center of the galaxy.  
334 Modern velocity measurements include significantly larger objects, galactic clusters, and smaller  
335 objects, dwarf galaxies. Yet, measurements along this regime are leveraging the Virial theorem  
336 with Newtonian potential energies. We know Newtonian gravity is not a comprehensive description  
337 of gravity. New observational techniques have been developed since 1978, and those are discussed  
338 in the following sections.

339 **2.3.2 Evidence for Dark Matter: Gravitational Lensing**

340 Modern evidence for dark matter comes from new avenues beyond stellar velocities. Grav-  
341 itational lensing from DM is a new channel from general relativity. General relativity predicts  
342 aberrations in light caused by massive objects. In recent decades we have been able to measure the  
343 lensing effects from compact objects and DM halos. Figure 2.2 shows how different massive ob-  
344 jects change the final image of a faraway galaxy resulting from gravitational lensing. Gravitational  
345 lensing developed our understanding of dark matter in two important ways.

346 Gravitational lensing provides additional compelling evidence for DM. The observation of two  
347 merging galactic clusters in 2006, shown in Figure 2.3, provided a compelling argument for DM  
348 outside the Standard Model. These clusters merged recently in astrophysical time scales. Galaxies  
349 and star cluster have mostly passed by each other as the likelihood of their collision is low. Therefore,  
350 these massive objects will mostly track the highest mass, dark and/or baryonic, density. Yet, the  
351 intergalactic gas is responsible for the majority of the baryonic mass in the systems [4]. These gas  
352 bodies will not phase through and will heat up as they collide together. The hot gas is located via  
353 x-ray emission from the cluster. Two observations of the clusters were performed independently of  
354 each other.

355 The first was the lensing of light around the galaxies due to their gravitational influences.  
356 When celestial bodies are large enough, the gravity they exert bends space and time itself. The  
357 warped space-time lenses light and will deflect in an analogous way to how glass lenses will bend

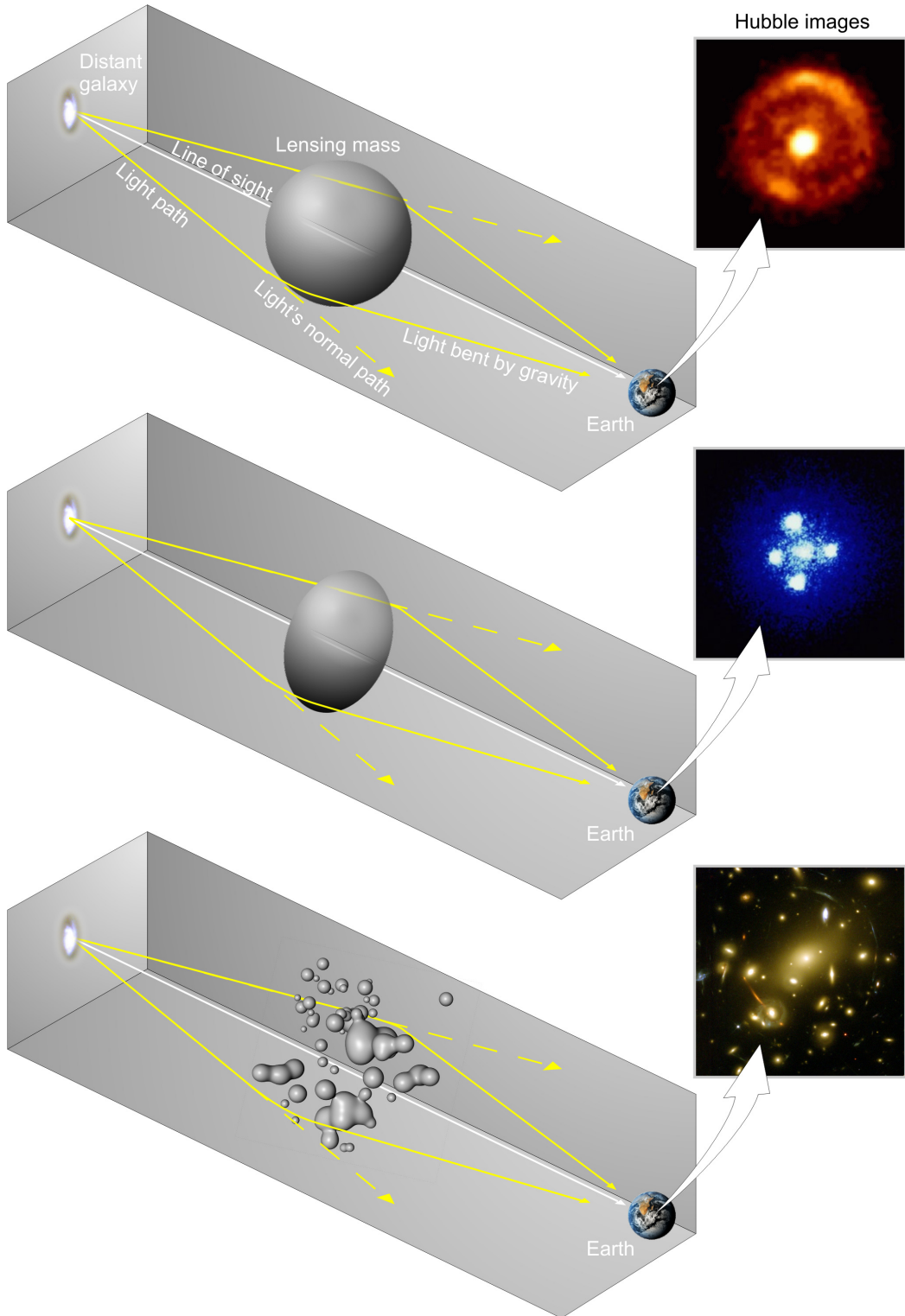


Figure 2.2 Light from distant galaxy is bent in unique ways depending on the distribution of mass between the galaxy and Earth. Yellow dashed lines indicate where the light would have gone if the matter were not present [8].

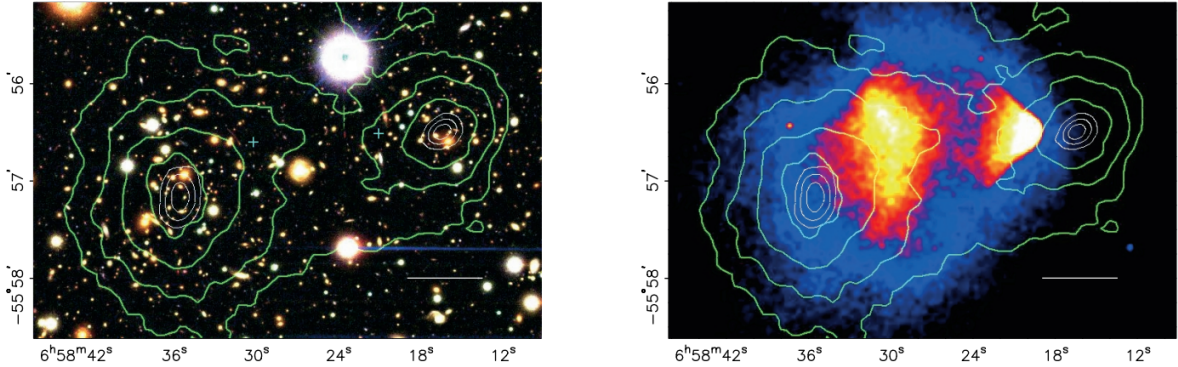


Figure 2.3 (left) Optical image of galactic cluster 1E0657-558. (right) X-ray image of the cluster with redder meaning hotter and higher baryon density. (both) Green contours are reconstruction of gravity contours from weak lensing. White rings are the best fit mass maxima at 68.3%, 95.5%, and 99.7% confidence. The matter maxima of the clusters are clearly separated from x-ray maxima. [9]

358 light, see Figure 2.2. With a sufficient understanding of light sources behind a massive object, we  
 359 can reconstruct the contours of the gravitational lenses. The gradient of the contours shown in  
 360 Figure 2.3 then indicates how dense the matter is and where it is.

361 The x-ray emission can then be observed from the clusters. Since these galaxies are mostly gas  
 362 and are merging, then the gas should be getting hotter. If they are merging, the x-ray emissions  
 363 should be the strongest where the gas is mostly moving through each other. Hence, X-ray emission  
 364 maps out where the gas is in the merging galaxy cluster.

365 The lensing and x-ray observations were done on the Bullet cluster featured on Figure 2.3.  
 366 The x-ray emissions do not align with the gravitational contours from lensing. The incongruence  
 367 in mass density and baryon density suggests that there is a lot of matter somewhere that does  
 368 not interact with light. Moreover, this dark matter cannot be baryonic [9]. The Bullet Cluster  
 369 measurement did not really tell us what DM is exactly, but it did give the clue that DM also does  
 370 not interact with itself very strongly. If DM did interact strongly with itself, then it would have been  
 371 more aligned with the x-ray emission [9]. There have been follow-up studies of galaxy clusters with  
 372 similar results. The Bullet Cluster and others like it provide a persuasive case against something  
 373 possibly amiss in our gravitational theories.

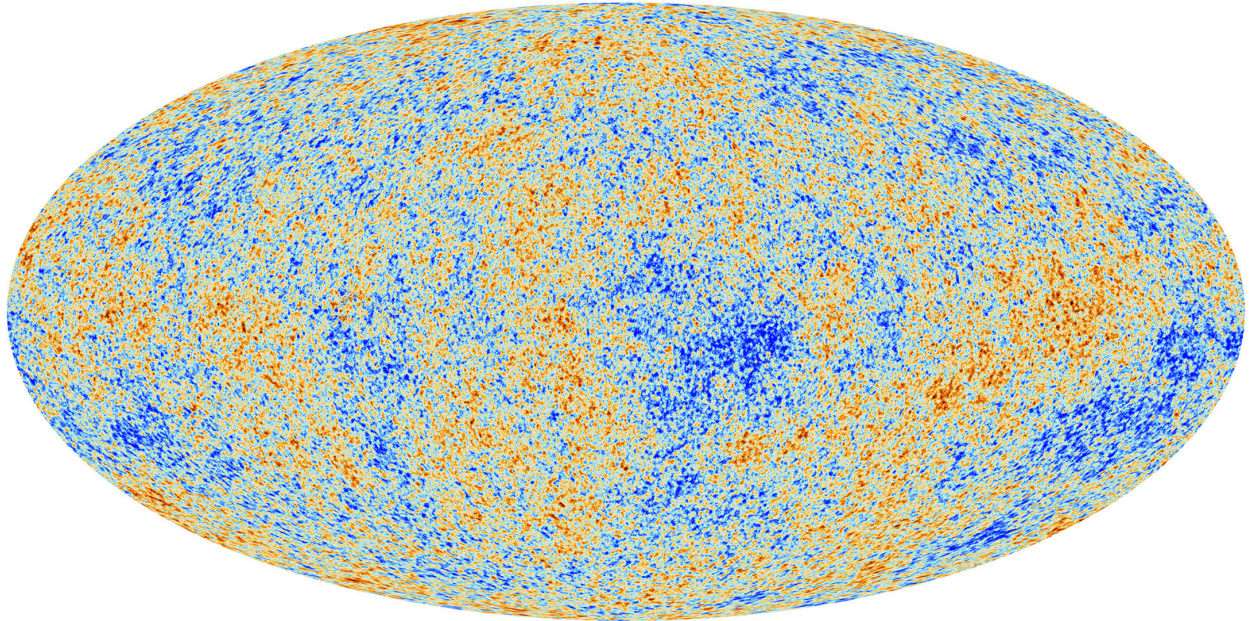


Figure 2.4 Plank CMB sky. Sky map features small variations in temperature in primordial light. These anisotropies are used to make inferences about the universe’s energy budget and developmental history. [10]

374     **2.3.3 Evidence for Dark Matter: Cosmic Microwave Background**

375       The Cosmic Microwave Background (CMB) is the primordial light from the early universe  
376       when Hydrogen atoms formed from the free electron and proton soup in the early universe. The  
377       CMB is the earliest light we can observe; released when the universe was about 380,000 years old.  
378       Then we look at how the simulated universes look like compared to what we see. Figure 2.4 is the  
379       most recent CMB image from the Plank satellite after subtracting the average value and masking the  
380       galactic plane [10]. Redder regions indicate a slightly hotter region in the CMB, and blue indicates  
381       colder. The intensity variations are on the order of 1 in 1000 with respect to the average value.

382       The Cosmic Microwave Background shows that the universe had DM in it from an incredibly  
383       early stage. To measure the DM, Dark Energy, and matter fractions of the universe from the CMB,  
384       the image is analyzed into a power spectrum, which shows the amplitude of the fluctuations as  
385       a function of spherical multipole moments.  $\Lambda$ CDM provides the best fit to the power spectra of  
386       the CMB as shown in Figure 2.5. The CMB power spectrum is quite sensitive to the fraction  
387       of each energy contribution in the early universe. Low  $l$  modes are dominated by variations  
388       in gravitational potential. Intermediate  $l$  emerge from oscillations in photon-baryon fluid from

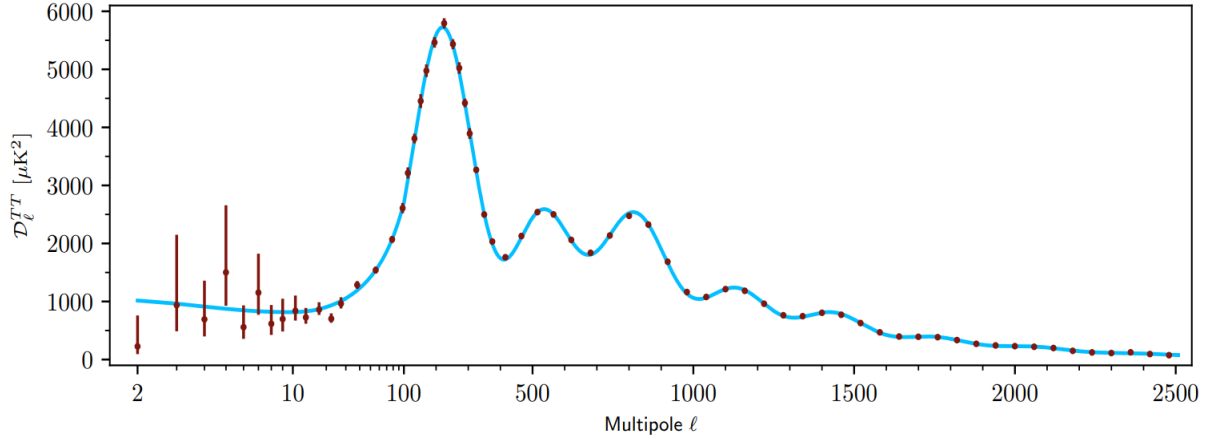


Figure 2.5 Observed Cosmic Microwave Background power spectrum as a function of multipole moment from Plank [10]. Blue line is best fit model from  $\Lambda$ CDM. Red points and lines are data and error, respectively.

389 competing baryon pressures and gravity. High  $l$  is a damped region from the diffusion of photons  
 390 during electron-proton recombination. [1]

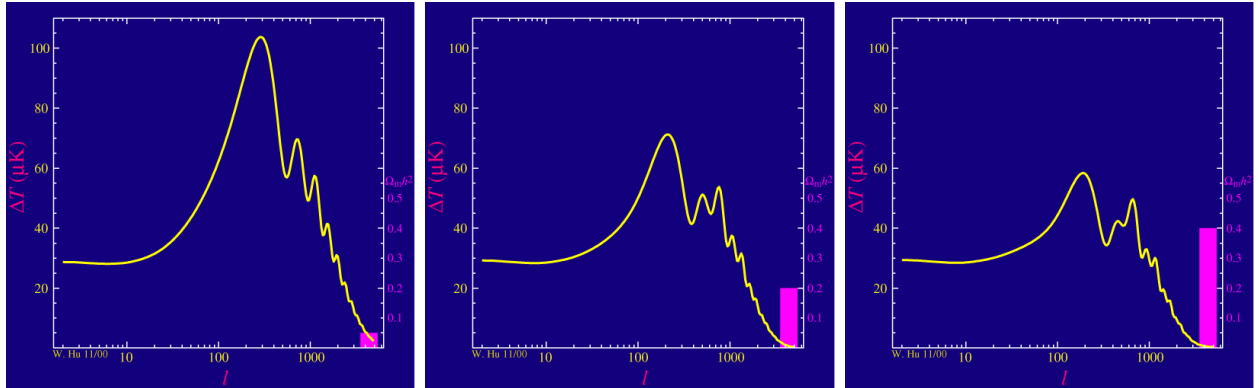


Figure 2.6 Predicted power spectra of CMB for different  $\Omega_m h^2$  values for fixed baryon density from [11]. (left) Low  $\Omega_m h^2$  increases the prominence of first and second peaks. (middle)  $\Omega_m h^2$  is most similar to the observed power spectrum. The second and third peaks are similar in height. (right)  $\Omega_m h^2$  is large which suppresses the first peak and raises the prominence of the third peak.

391 The harmonics would look quite different for a universe with less DM. Figure 2.6 demonstrates  
 392 the effect  $\Omega_m h^2$  has on the expected power spectrum for fixed baryon matter density. [11] Sweeping  
 393  $\Omega_m h^2$  in this way clearly shows the effect dark matter has on the CMB power spectrum. The  
 394 observations fit well with the  $\Lambda$ CDM model, and the derived fractions are as follows. The matter  
 395 fraction:  $\Omega_m = 0.3153$ ; and the baryon fraction:  $\Omega_b = 0.04936$  [10]. Plank's observations also  
 396 provide a measure of the Hubble constant,  $H_0$ .  $H_0$  especially has seen a growing tension in the

397 past decade that continues to deepened with observations from instruments like the James Webb  
398 Telescope [12, 13]. As Hubble tensions deepen, we may find that perhaps  $\Lambda$ **CDM**, despite its  
399 successes, is missing some critical physics.

400 Overall, the Newtonian motion of stars in galaxies, weak lensing from galactic clusters, and  
401 power spectra from primordial light form a compelling body of research in favor of dark matter.  
402 It takes another leap of theory and experimentation to make observations of DM that are non-  
403 gravitational in nature. In Section 2.3, the evidence for DM implies strongly that the DM is matter  
404 and not a lost parameter in the gravitational fields between massive objects. Finally, if we take one  
405 axiom: that this matter has quantum behavior, such as being described by some Bohr wavelength  
406 and abiding by some fermion or boson statistics; then we arrive at particle dark matter. One particle  
407 DM hypothesis is the Weakly Interacting Massive Particle (WIMP). This DM candidate theory is  
408 discussed further in the next section and is the focus of this thesis.

409 **2.4 Searching for Dark Matter: Particle DM**

410 Section 2.4 shows the Standard Model of particle physics and is currently the most accurate  
411 model for the dynamics of fundamental particles like electrons and photons. The current status  
412 of the SM does not have a viable DM candidate. When looking at the standard model, we can  
413 immediately exclude any charged particle because charged particles interact strongly with light.  
414 Specifically, this will rule out the following charged, fundamental particles:  $e, \mu, \tau, W, u, d, s, c, t, b$   
415 and their corresponding antiparticles. Recalling from Section 2.2 that DM must be long-lived and  
416 stable over the age of the universe which excludes all SM particles with decay half-lives at or shorter  
417 than the age of the universe. The lifetime constraint additionally eliminates the  $Z$  and  $H$  bosons.  
418 Finally, the candidate DM needs to be somewhat massive. Recall from Section 2.2 that DM is cold  
419 or not relativistic through the universe. This eliminates the remaining SM particles:  $\nu_{e,\mu,\tau}, g, \gamma$  as  
420 DM candidates. Because there are no DM candidates within the SM, the DM problem strongly  
421 hints to physics beyond the SM (BSM).

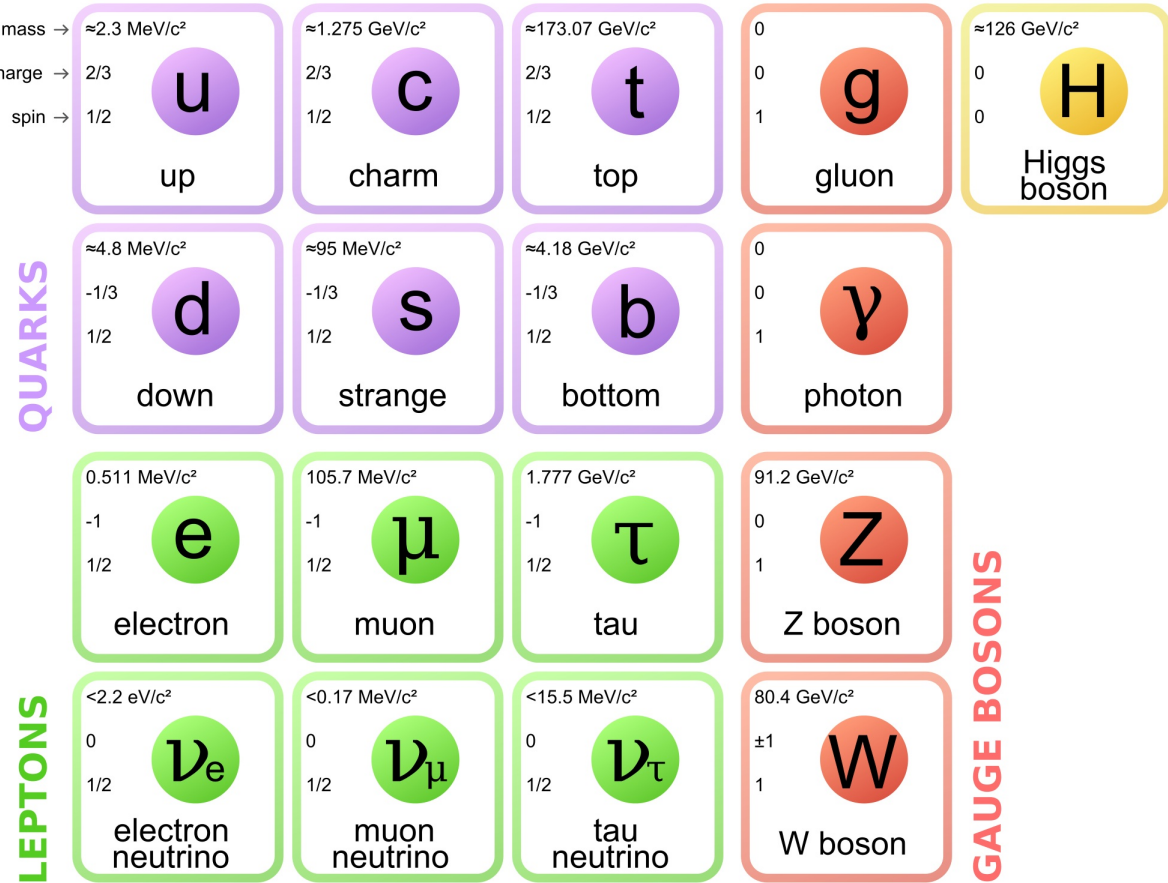


Figure 2.7 The Standard Model (SM) of particle physics. Figure taken from <http://www.quantumdiaries.org/2014/03/14/the-standard-model-a-beautiful-but-flawed-theory/>

#### 422 2.4.1 Shake it, Break it, Make it

423 When considering DM that couples in some way with the SM, the interactions are roughly  
 424 demonstrated by interaction demonstrated in Figure 2.8. The figure is a simplified Feynman  
 425 diagram where the arrow of time represents the interaction modes of: **Shake it, Break it, Make it.**

426 **Shake it** refers to the direct detection of dark matter. Direct detection interactions start with  
 427 a free DM particle and an SM particle. The DM and SM interact via elastic or inelastic collision  
 428 and recoil away from each other. The DM remains in the dark sector and imparts some momentum  
 429 onto the SM particle. The hope is that the momentum imparted onto the SM particle is sufficiently  
 430 high enough to pick up with extremely sensitive instruments. Because we cannot create the DM in  
 431 the lab, a direct detection experiment must wait until DM is incident on the detector. Most direct  
 432 detection experiments are therefore placed in low-background environments with inert detection

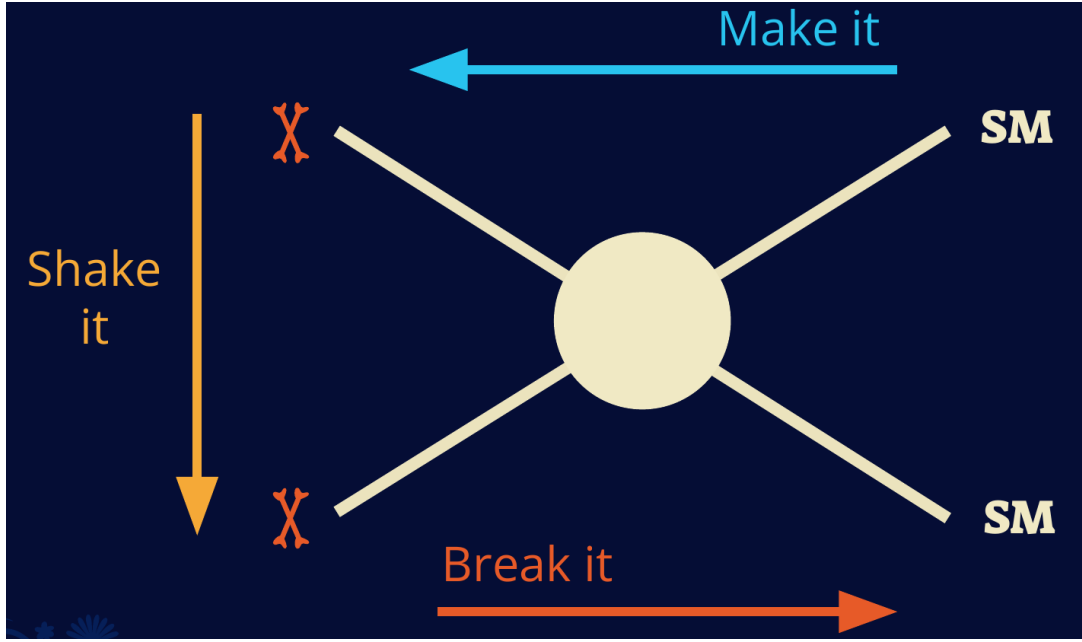


Figure 2.8 Simplified Feynman diagram demonstrating different ways DM can interact with SM particles. The 'X's refer to the DM particles whereas the SM refer to fundamental particles in the SM. The large circle in the center indicates the vertex of interaction and is purposely left vague. The colored arrows refer to different directions of time as well as their respective labels. The arrows indicate the initial and final state of the DM -SM interaction in time.

433 media like the noble gas Xenon. [14]

434 **Make it** refers to the production of DM from SM initial states. The experiment starts with  
 435 particles in the SM. These SM particles are accelerated to incredibly high energies and then collide  
 436 with each other. In the confluence of energy, DM hopefully emerges as a byproduct of the SM  
 437 annihilation. Often it is the collider experiments that are energetic enough to hypothetically produce  
 438 DM. These experiments include the world-wide collaborations ATLAS and CMS at CERN where  
 439 proton collide together at extreme energies. The DM searches, however, are complex. DM likely  
 440 does not interact with the detectors and lives long enough to escape the detection apparatus of  
 441 CERN's colliders. This means any DM production experiment searches for an excess of events  
 442 with missing momentum or energy in the events. An example event with missing transverse  
 443 momentum is shown in Figure 2.9. The missing momentum with no particle tracks implies a  
 444 neutral particle carried the energy out of the detector. However, there are other neutral particles  
 445 in the SM, like neutrons or neutrinos, so any analysis has to account for SM signatures of missing

446 momentum. [15]

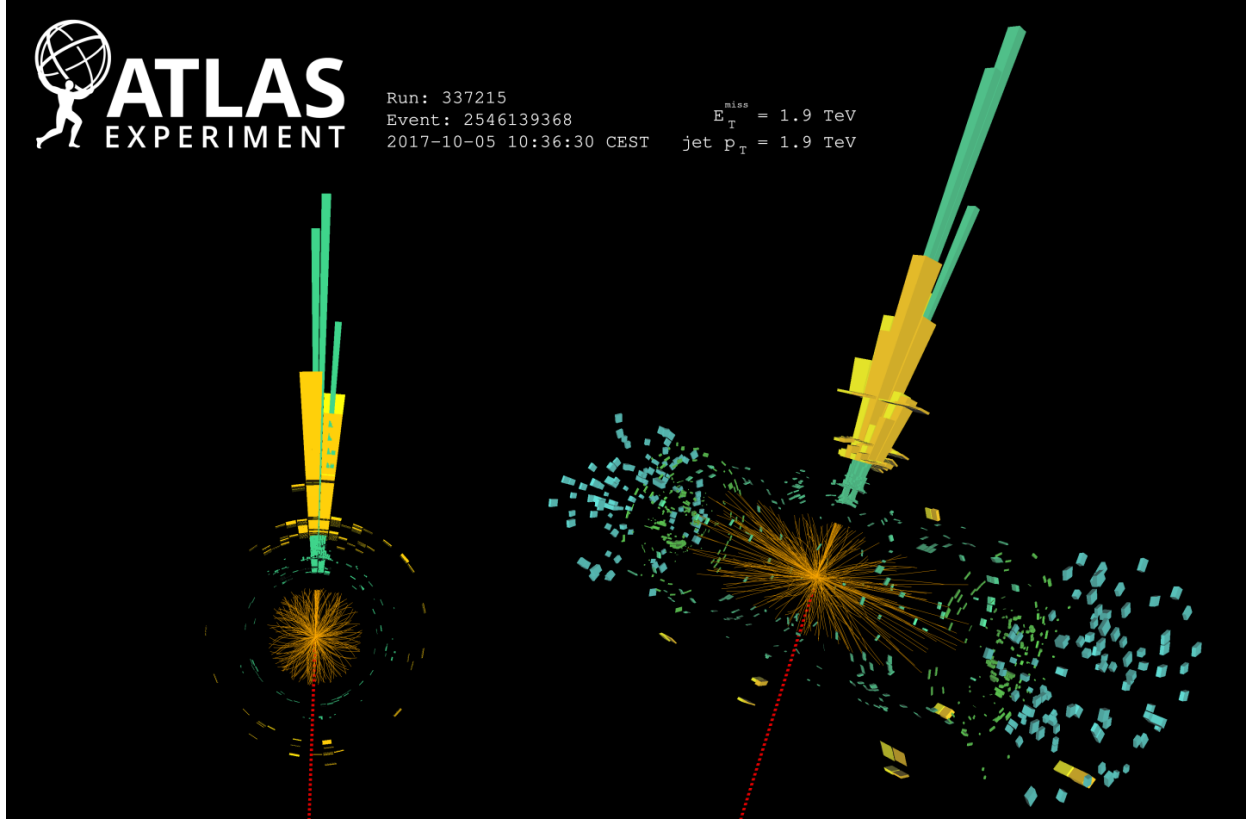


Figure 2.9 A single jet event in ATLAS detector from 2017 [16]. Jet momentum was observed to be 1.9 TeV. Missing transverse momentum was observed to be 1.9 TeV compared to the initial transverse momentum of the event was 0. Implied MET is traced by a red dashed line in event display.

#### 447 2.4.2 Break it: Standard Model Signatures of Dark Matter through Indirect Searches

448 **Break it** refers to the creation of SM particles from the dark sector, and it is the primary focus  
449 of this thesis. The interaction begins with DM or in the dark sector. The hypothesis is that this  
450 DM will either annihilate with itself or decay and produce an SM byproduct. This method is  
451 often referred to as the Indirect Detection of DM because we have no lab to directly control or  
452 manipulate the DM. Therefore, most indirect DM searches are performed using observations of  
453 known DM densities among the astrophysical sources. The strength is that we have the whole of the  
454 universe and its 13.6-billion-year lifespan to use as a detector and particle accelerator. Additionally,  
455 locations of dark matter are well cataloged since it was astrophysical observations that presented

456 the problem of DM in the first place.

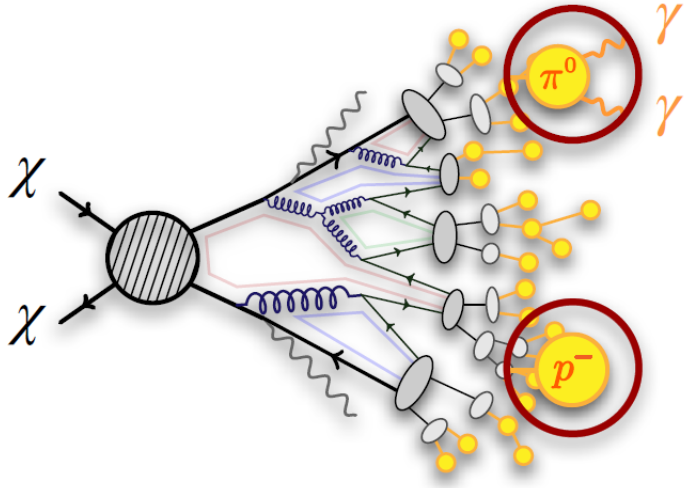


Figure 2.10 More detailed pseudo-Feynman diagram of particle cascade from dark matter annihilation into 2 quarks. The quarks hadronize and down to stable particles like  $\gamma$  or the anti-proton ( $p^-$ ). Diagram pulled from ICRC 2021 presentation on DM annihilation search [17].

457 However, anything can happen in the universe. There are many difficult to deconvolve back-  
458 grounds when searching for DM. One prominent example is the galactic center. We know the  
459 galactic center has a large DM content because of stellar kinematics in our Milky Way and DM halo  
460 simulations. Yet, any signal from the galactic center is challenging to parse apart from the extreme  
461 environment of our supermassive black hole, unresolved sources, and diffuse emission from the  
462 interstellar medium [18]. Despite the challenges, any DM model that yields evidence in the other  
463 two observation methods, **Shake it or Make it** must be corroborated with indirect observations of  
464 the known DM sources. Without corroborating evidence, DM observation in the lab is hard-pressed  
465 to demonstrate that it is the model contributing to the DM seen at the universal scale.

466 In the case of WIMP DM, signals are described in terms of primary SM particles produced  
467 from DM decay or annihilation. The SM initial state particles are then simulated down to stable  
468 final states such as the  $\gamma$ ,  $\nu$ ,  $p$ , or  $e$  which can traverse galactic lengths to reach Earth.

469 Figure 2.10 shows the quagmire of SM particles that emerges from SM initial states that are not  
470 stable [17]. There are many SM particles with varying energies that can be produced in such an

471 interaction. For any arbitrary DM source and stable SM particle, the SM flux from DM annihilating  
 472 to a neutral particle in the SM,  $\phi$ , from a region in the sky is described by the following.

$$\frac{d\Phi_\phi}{dE_\phi} = \frac{\langle\sigma v\rangle}{8\pi m_\chi^2} \frac{dN_\phi}{dE_\phi} \times \int_{\text{source}} d\Omega \int_{l.o.s} \rho_\chi^2 dl(r, \theta') \quad (2.4)$$

473 In Equation (7.1),  $\langle\sigma v\rangle$  is the velocity-weighted annihilation cross-section of DM to the SM.  $m_\chi$   
 474 refers to the mass of DM, noted with Greek letter  $\chi$ .  $\frac{dN_\phi}{dE_\phi}$  is the N particle flux weighted by the  
 475 particle energy. An example is provided in Figure 2.11 for the  $\gamma$  final state. The integrated terms  
 476 are performed over the solid angle,  $d\Omega$ , and line of sight, l.o.s.  $\rho$  is the density of DM for a  
 477 location  $(r, \theta')$  in the sky. The terms left of the ' $\times$ ' are often referred to as the particle physics  
 478 component. The terms on the right are referred to as the astrophysical component. For decaying  
 479 DM, the equation changes to...

$$\frac{d\Phi_\phi}{dE_\phi} = \frac{1}{4\pi\tau m_\chi} \frac{dN_\phi}{dE_\phi} \times \int_{\text{source}} d\Omega \int_{l.o.s} \rho_\chi dl(r, \theta') \quad (2.5)$$

480 In Equation (2.5),  $\tau$  is the decay lifetime of the DM. Just as in Equation (7.1), the left and  
 481 right terms are the particle physics and the astrophysical components respectively. The integrated  
 482 astrophysical component of Equation (7.1) is often called the J-Factor. Whereas the integrated  
 483 astrophysical component of Equation (2.5) is often called the D-Factor.

484 Exact DM  $\text{DM} \rightarrow \text{SM SM}$  branching ratios are not known, so it is usually assumed to go 100%  
 485 into an SM particle/anti-particle. Additionally, when a DM annihilation or decay produces one of  
 486 the neutral, long-lived SM particles ( $\nu$  or  $\gamma$ ), the particle is traced back to a DM source. For DM  
 487 above GeV energies, there are very few SM processes that can produce particles with such a high  
 488 energy. Seeing such a signal would almost certainly be an indication of the presence of dark matter.  
 489 Fortunately, the universe provides us with the largest volume and lifetime ever for a particle physics  
 490 experiment.

## 491 2.5 Sources for Indirect Dark Matter Searches

492 The first detection of DM relied on optical observations. Since then, we have developed new  
 493 techniques to find DM dense regions. As described in Section 2.3.1, many DM dense regions were  
 494 through observing galactic rotation curves. Our Milky Way galaxy is among DM dense regions

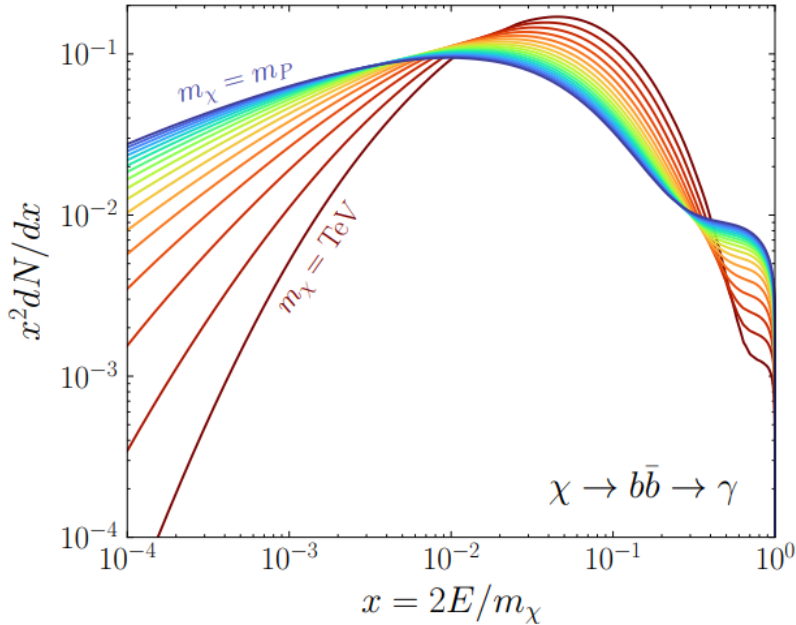


Figure 2.11 Dark Matter (DM) decay spectrum for  $b\bar{b}$  initial state and  $\gamma$  final state. Redder spectra are for larger DM masses. Bluer spectra are light DM masses.  $x$  is a unitless factor defined as the ratio of the mass of DM,  $m_\chi$ , and the final state particle energy  $E_\gamma$ . Figure from [19].

discovered, and it is the largest nearby DM dense region to look at. Additionally, the DM halo surrounding the Milky Way is clumpy [18]. There are regions in the DM halo of the Milky Way that have more DM than others that have captured gas over time. These sub-halos were dense enough collapse gas and form stars. These apparent sub galaxies are known as dwarf spheroidal galaxies and are the main sources studied in this thesis. Each source type comes with different trade-offs. Galactic Center studies will be very sensitive to the assumed distribution of DM. The central DM density can vary substantially as demonstrated in Figure 2.12. At distances close to the center of the galaxy, or small  $r$ , the differences in DM densities can be 3-4 orders of magnitude. Searches toward the galactic center will therefore be quite sensitive to the assumed DM distribution.

Searches toward Dwarf Spheroidal Galaxies (dSph's) suffer from uncertainties in the DM density less than the galactic center studies. This is mostly from their diminutive size being smaller than the angular resolution of most  $\gamma$ -ray observatories [18]. The DM content dSph's are typically determined with the Virial theorem, Equation (2.1), and are usually majority DM [18] in mass. DSph's tend to be ideal sources to look at for DM searches. Their environments are quiet with little

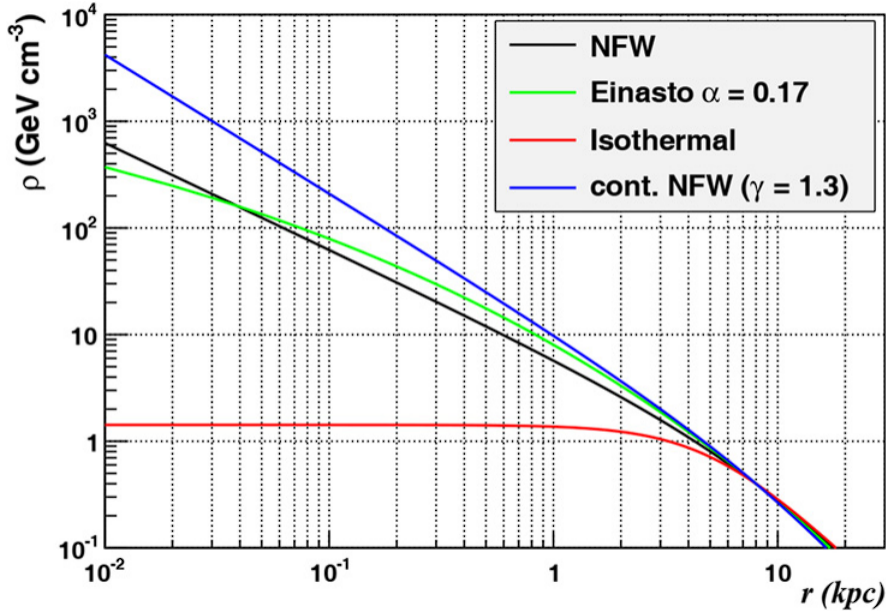


Figure 2.12 Different dark matter density profiles compared. Some models produce exceptionally large densities at small  $r$  [20].

509 astrophysical background. Unlike the galactic center, the most active components of dSph's are the  
 510 stars within them versus a violent accretion disc around a black hole. All this together means that  
 511 dSph's are among the best sources to look at for indirect DM searches. dSph's are the targets of  
 512 focus for this thesis.

## 513 2.6 Multi-Messenger Dark Matter

514 Astrophysics entered a new phase in the past few decades that leverages our increasing sensitivity  
 515 to SM channels and general relativity (GR). Up until the 21st century, astrophysical observations  
 516 were performed with photons ( $\gamma$ ) only. Astrophysics with this 'messenger' is fairly mature now.  
 517 Novel observations of the universe have since only adjusted the sensitivity of the wavelength of  
 518 light that is observed except at MeV energies. Gems like the CMB [10], and more have ultimately  
 519 been observations of different wavelengths of light. Multi-messenger astrophysics proposes using  
 520 other SM particles such the  $p^{+-}$ , or  $\nu$  or gravitation waves predicted by general relativity.

521 The experiment LIGO had a revolutionary discovery in 2016 with the first detection of a binary  
 522 black hole merger [21]. This opened the collective imagination to observing the universe through  
 523 gravitational waves. There has also been a surge of interest in the neutrino ( $\nu$ ) sector. IceCube

524 demonstrated that we are sensitive to neutrinos in regions that correlate with significant photon  
 525 emission like the galactic plane [22]. Neutrinos, like gravitational waves and light, travel mostly  
 526 unimpeded from their source to our observatories. This makes pointing to the originating source  
 527 of these messengers much easier than it is for cosmic rays which are deflected from their source by  
 528 magnetic fields.

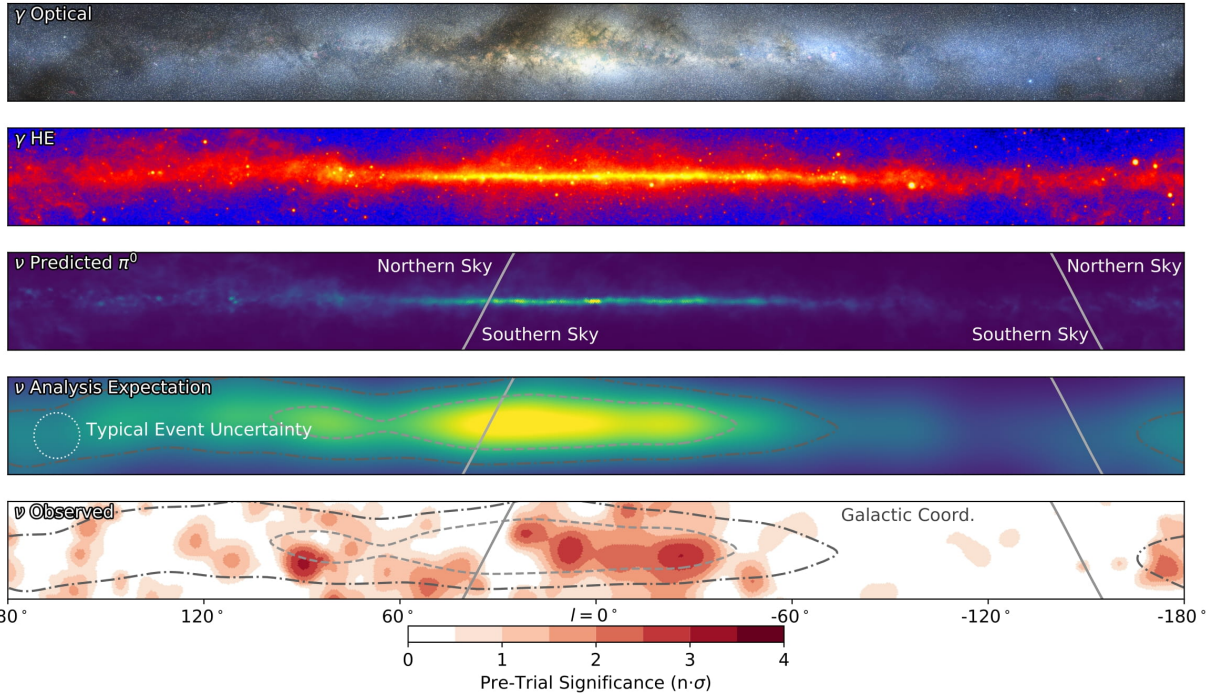


Figure 2.13 The Milky Way Galaxy in photons ( $\gamma$ ) and neutrinos ( $\nu$ ) [22]. The Galactic center is at  $l=0^\circ$  and is the brightest region in all panels. (top) An Optical color image of the Milky Way galaxy seen from Earth. Clouds of gas and dust obscure some light from stars. (2nd down) Integrated flux of  $\gamma$ -rays observed by the Fermi-LAT telescope [23]. (middle) Expected neutrino emission that corresponds with Fermi-LAT observations. (2nd up) Expected neutrino emission profile after considering detector systematics of IceCube. (bottom) Observed neutrino emission from region of the galactic plane. Substantial neutrino emission was detected.

529 The IceCube collaboration recently published a groundbreaking result of the Milky Way in  
 530 neutrinos. The recent result from IceCube, shown in Figure 2.13, proves that we can make  
 531 observations under different messenger regimes. The top two panels show the appearance of the  
 532 galactic plane to different wavelengths of light. Some sources are more apparent in some panels,  
 533 while others are not. This new channel is powerful because neutrinos are readily able to penetrate  
 534 through gas and dust in the Milky Way. This new image also refines our understanding of how high

535 energy particles are produced. For example, the fit to IceCube data prefers neutrino production  
 536 from the decay of  $\pi^0$  [22].

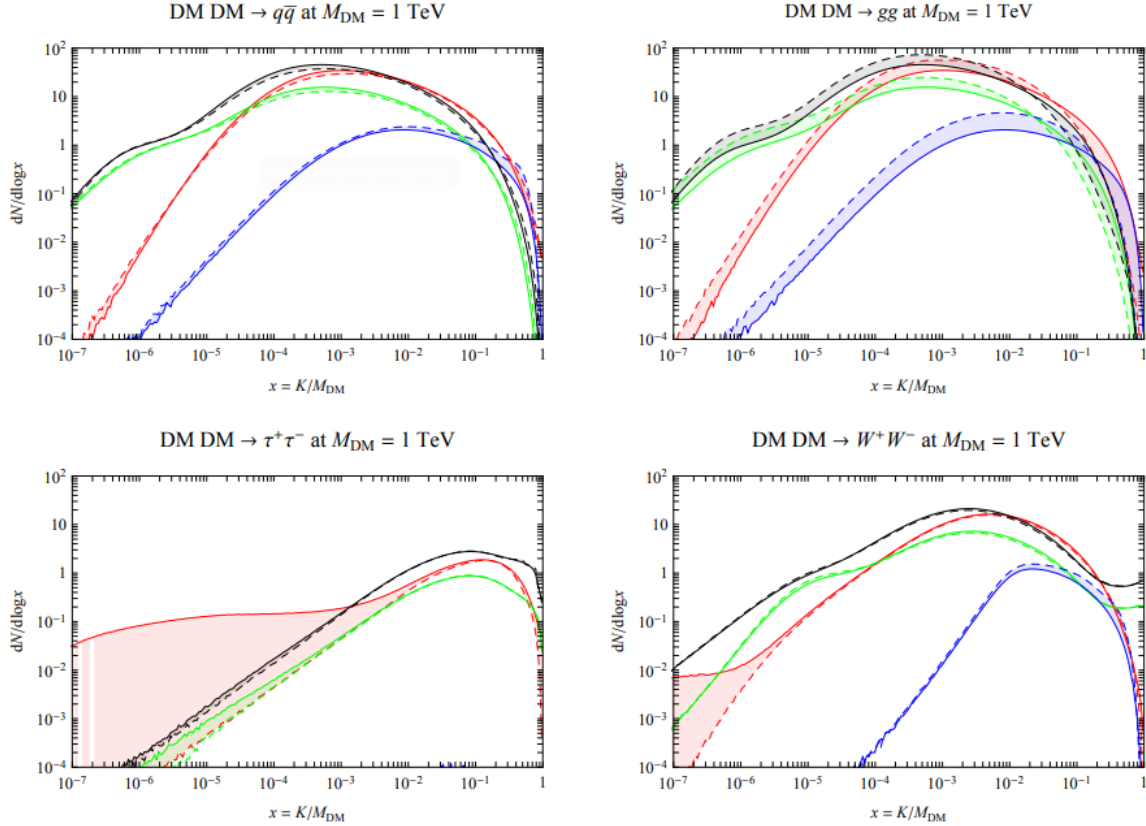


Figure 2.14 Dark Matter annihilation spectra for different final state particle and standard model annihilation channels [24]. Photons (red),  $e^\pm$  (green),  $\bar{p}$  (blue),  $\nu$  (black).

537 Exposing our observations to more cosmic messengers greatly increases our sensitivity to  
 538 rare processes. In the case of DM, Figure 2.14, there are many SM particles produced in DM  
 539 annihilation. Among the final state fluxes are gammas and neutrinos. Charged particles are also  
 540 produced however they would not likely make it to Earth since they will be deflected by magnetic  
 541 fields between the source and Earth. This means observatories that can see the neutral messengers  
 542 are especially good for DM searches and for combining data for a multi-messenger DM search.

## CHAPTER 3

### 543 MULTIMESSENGER ASTROPHYSICS: DETECTING HIGH ENERGY NEUTRAL 544 MESSENGERS

#### 545 3.1 Introduction

546 Before the 20th century, all asttrophysics observations were optical in nature. We litterly only  
547 saw things with highly magnified optical observations. Then we discovered cosmic rays. cosmic  
548 rays are charged particles, typically naked protons or H+. This was seen by Victor Hess in 19??.  
549 Around the same time we discovered neutrinos from beta decay. Sometime around 1950 we started  
550 to build neutrino detectors which were mostly sensitive to neutrinos from the sun. Finally, it was  
551 theorized that compact objects like black holes and neutron stars would create waves in space-time  
552 when they experience mergers or collisions.

553 In the 21st century, we have developed new observation techniques and detectors that are no only  
554 sensitive to these four messengers - photons ( TODO: photon), neutrinos ( TODO: nu), Cosmic  
555 Rays (CR), and Gravitational Wave (WV) - we're collect high energy versions of these events.  
556 For the standad model particles, we're now sensitive to all messengers above the MeV eneryg  
557 range. Additionally, the GW's were sensitive to are in the stellar mass black hole region and above  
558 within our galactic neighborhood. This means were becoming sensitive to the fundamental physics  
559 occuring within the universe and we can rely on the universe as a TeV+ particle accelerator. We  
560 also have the abaility to correlate high energy events across messengers and gain new insights on  
561 the processes that occur in our universe.

562 This thesis focuses on very high energy (VHE) gamma rays and neutrinos. These can both be  
563 observed through the water cherenkov detection technique altho not exclusively. Methods on how  
564 to detect and observe these neutral messengers are discussed Section 3.3 and Section 3.4

#### 565 3.2 Charged Particles in a Medium

566 For high enery gamma-rays and neutrinos, we can exploit the same effect that charged particles  
567 have with water. This effect is known as Cherenkov radiation. Cherenkov Radiation occurs when a  
568 charged particle, usually electrons ( $e$ ) or muons ( $\mu$ ), traverse a medium, like water, faster than the

569 speed of light in that medium. This is similar to sonic boom where an object moves through air  
570 faster than the speed of sound in air. Cherenkov radiation can therefore be thought of as an 'optic  
571 boom'. Many astro-particle physics experiments will use water as the medium as because water  
572 has a unique set of properties ideal for charged particle tracking.



Figure 3.1 TODO: Show a nuclear reactor with cherenkov radiation[NEEDS A SOURCE][FACT CHECK THIS]

573 The frequency of light emitted due to cherenkov radiation follows the equation:

$$INSERT\ Cherenkov\ wavelength\ calc\ HERE. \quad (3.1)$$

574 The absorption spectra is shown in the following figure:

575 **3.3 Photons ( $\gamma$ )**

576 **3.4 Neutrinos ( $\nu$ )**

577 **3.5 Opportunities to Combine for Dark Matter**



Figure 3.2 TODO: absorption spectrum of liquid and solid water[NEEDS A SOURCE][FACT CHECK THIS]

## CHAPTER 4

578

### HIGH ALTITUDE WATER CHERENKOV (HAWC) OBSERVATORY

579 **4.1 The Detector**

580 **4.2 Events Reconstruction and Data Acquisition**

581 **4.2.1 G/H Discrimination**

582 **4.2.2 Angle**

583 **4.2.3 Energy**

584 **4.3 Remote Monitoring**

585 **4.3.1 ATHENA Database**

586 **4.3.2 HOMER**

587

## CHAPTER 5

### ICECUBE NEUTRINO OBSERVATORY

588 **5.1 The Detector**

589 **5.2 Events Reconstruction and Data Acquisition**

590 **5.2.1 Angle**

591 **5.2.2 Energy**

592 **5.3 Northern Test Site**

593 **5.3.1 PIgeon remote dark rate testing**

594 **5.3.2 Bulkhead Construction**

## CHAPTER 6

### COMPUTATIONAL TECHNIQUES IN PARTICLE ASTROPHYSICS

596 **6.1 Neural Networks for Gamma/Hadron Separation**

597 **6.2 Parallel Computing for Dark Matter Analyses**

## CHAPTER 7

### GLORY DUCK: MULTI-WAVELENGTH SEARCH FOR DARK MATTER ANNIHILATION TOWARDS DWARF SPHEROIDAL GALAXIES

#### 600 7.1 Introduction

601 The field of astrophysics now has several instruments and observatories sensitive to high  
 602 energy gamma-rays. The energy sensitivity for the modern gamma-ray program spans many orders  
 603 of magnitude. Figure 7.1 demonstrates these similar sensitivities across energies for the five  
 604 experiments: Fermi-LAT, HAWC, HESS, MAGIC, and VERITAS.

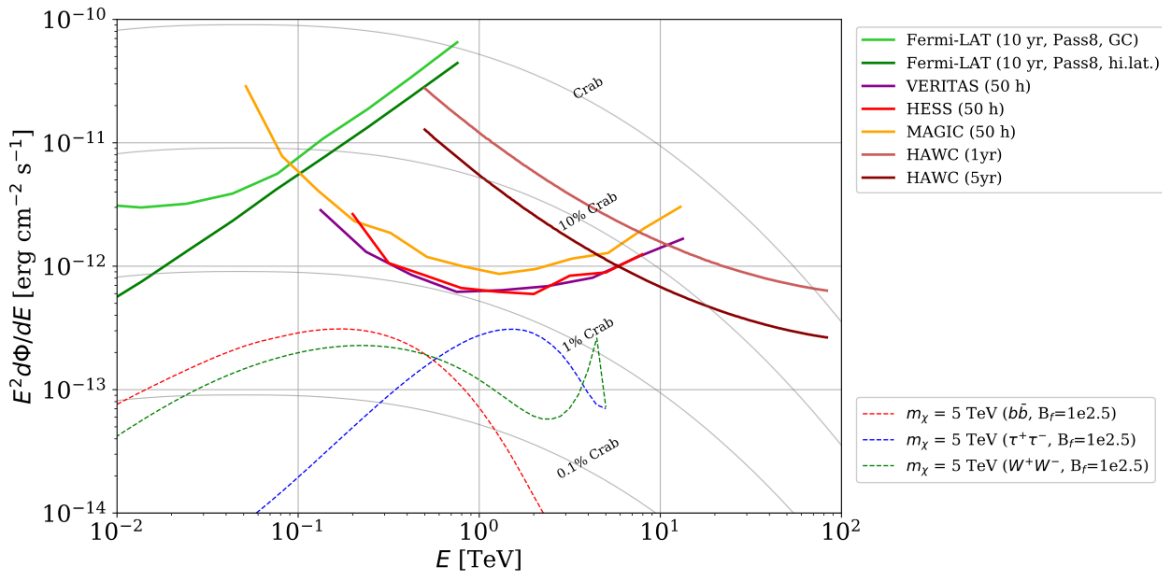


Figure 7.1 [NEEDS A SOURCE]Sensitivities of five gamma-ray experiments compared to percentages of the Crab nebula’s emission and dark matter annihilation. Solid lines present estimated sensitivities to power law spectra [FACT CHECK THIS]for each experiment. Green lines are Fermi-LAT sensitivities where lighter green is the sensitivity to the galactic center and dark green is its sensitivity to higher declinations. Orange, red, and purple solid lines represent the MAGIC, HESS, and VERITAS 50 hour sensitivities respectively. The maroon and brown lines are the HAWC 1 year and 5 year sensitivities. Across four decades of gamma-ray energy, these experiments have similar sensitivities on the order  $10^{-12}$  erg cm $^{-2}$ s $^{-1}$ . The dotted lines are estimated dark matter fluxes assuming  $m_\chi = 5$  TeV DM annihilating to bottom quarks (red), tau leptons (blue), and W bosons (green). Faded gray lines outline percentage flux of the Crab nebula.

605 Each of the five experiments featured in Figure 7.1 have independently searched for DM  
 606 annihilation from dwarf spheroidal galaxies (dSph) and set limits. Intriguingly, there are regions of  
 607 substantial overlap in their energy sensitivities. This clearly motivates an analysis that combines data

608 from these five. Each experiment has unique gamma-ray detection methods and their weaknesses  
609 and strengths can be leveraged with each other. The HAWC gamma-ray observatory is extensively  
610 introduced in chapter 4, so it is not introduced here. A brief description of the remaining experiments  
611 are in the following paragraphs.

612 The Large Area Telescope (LAT) is a pair conversion telescope mounted on the NASA Fermi  
613 satellite in orbit  $\sim$ 550 km above the Earth [25]. LAT's field of view covers about 20% of the  
614 whole sky, and it sweeps the whole sky approximately every 3 hours. LAT's gamma-ray energy  
615 sensitivity ranges from 20 MeV up to 1 TeV. Previous DM searches towards dSphs using Fermi-LAT  
616 are published in [26] and [27]

617 The High Energy Spectroscopic System (HESS), Major Atmospheric Gamma Imaging  
618 Cherenkov (MAGIC), and Very Energetic Radiation Imaging Telescope Array System (VERI-  
619 TAS) are arrays of Imaging Atmospheric Cherenkov Telescopes (IACT). These telescopes observe  
620 the Cherenkov light emitted from gamma-ray showers in the Earth's atmosphere. The field of  
621 view for these telescopes is no larger than  $5^\circ$  with energy sensitivities ranging from 30 GeV up  
622 to 100 TeV [28, 29, 30]. IACTs are able to make precise observations in selected regions of the  
623 sky, however can only be operated in ideal dark conditions. HESS's observations of the dwarves  
624 Sculptor and Carina were between January 2008 and December 2009. HESS's observations of  
625 Coma Berenices were from 2010 to 2013, and Fornax was observed in 2010 [31, 32, 33]. MAGIC  
626 provided deep observations of Segue1 between 2011 and 2013 [34]. MAGIC also provides data  
627 for three dwarves: Coma Berenices, Draco, and Ursa Major II where observations were made  
628 in: January - June 2019 [35], March - September 2018 [35], and 2014 - 2016 [36] respectively.  
629 VERITAS provided data for Boötes I, Draco, Segue 1, and Ursa Minor from 2009 to 2016 [37].

630 This chapter presents the Glory Duck analysis, the name given for the search for dark matter  
631 annihilation from dSph by combining data from the five gamma-ray observatories: Fermi-LAT,  
632 HAWC, HESS, MAGIC, and VERITAS. Specifically, the methods in analysis and modeling are  
633 presented for the HAWC gamma-ray observatory. This work was published to the Journal of  
634 Cosmology and Astroparticle Physics and presented at the International Cosmic Ray Conference

635 in 2019, 2021, and 2023 [38, 39, 40] and others.

636 **7.2 Dataset and Background**

637 This section enumerates the data and background methods used for HAWC’s study of dSphs.  
638 Section 7.2.1 and Section 7.2.2 are most useful for fellow HAWC collaborators looking to replicate  
639 the Glory Duck analysis.

640 **7.2.1 Itemized HAWC files**

- 641 • Detector Resolution: `response_aerie_svn_27754_systematics_best_mc_test_no`  
642 `broadpulse\_10pctlogchargesmearing_0.63qe_25kHzNoise_run5481_curvatu`  
643 `re0_index3.root`
- 644 • Data Map: `maps-20180119/liff/maptree_1024.root`
- 645 • Spectral Dictionary: `DM_CirrelliSpectrum_dict_gammas.npy`
- 646 • Analysis wiki: [https://private.hawc-observatory.org/wiki/index.php/Glory\\_Duck\\_Multi-Experiment\\_Dark\\_Matter\\_Search](https://private.hawc-observatory.org/wiki/index.php/Glory_Duck_Multi-Experiment_Dark_Matter_Search)

648 **7.2.2 Software Tools and Development**

649 This analysis was performed using HAL and 3ML [41, 42], in Python version 2. I built software  
650 to implement the *A Poor Particle Physicist Cookbook for Dark Matter Indirect Detection* (PPPC)  
651 [43] DM spectral model and dSphs spatial model from [44] for HAWC analysis. A NumPy version  
652 of this dictionary was made for both Py2 and Py3. The code base for creating this dictionary is  
653 linked on my GitLab sandbox:

- 654 • Py2: [Dictionary Generator \(Deprecated\)](#)
- 655 • Py3: [PPPC2Dict](#)

656 The analysis was performed using the  $f_{\text{hit}}$  framework performed in the HAWC Crab paper  
657 [41]. The Python2 NumPy dictionary file for gamma-ray final states is `dmCirSpecDict.npy`. The  
658 corresponding Python3 file is `DM_CirrelliSpectrum_dict_gammas.npy`. These files can also

659 be used for decay channels and the PPPC describes how [43]. All other software used for data  
660 analysis, DM profile generation, and job submission to SLURM are also kept in my sandbox for  
661 [the Glory Duck](#) project.

662 **7.2.3 Data Set and Background Description**

663 The HAWC data maps used for this analysis contain 1017 days of data between runs 2104  
664 (2014-11-26) and 7476 (2017-12-20). They were generated from pass 4.0 reconstruction. The  
665 analysis is performed using the  $f_{hit}$  energy binning scheme with bins (1-9) similar to what was done  
666 for the Crab and previous HAWC dSph analysis [41, 45]. Bin 0 was excluded as it has substantial  
667 hadronic contamination and poor angular resolution.

668 This analysis was done on dwarf spheroidal (dSph) galaxies because of their large DM mass  
669 content relative to baryonic mass. We consider the following to estimate the background to this  
670 study.

- 671 • The dSphs are small in HAWC’s field of view, so the analysis is not sensitive to large or small  
672 scale anisotropies.
- 673 • The dSphs used in this analysis are off the galactic plane.
- 674 • The dSphs are baryonically faint relative to their expected dark matter content and are not  
675 expected to contain high energy gamma-ray sources.

676 Therefor we make no additional assumptions on the background from our sources and use  
677 HAWC’s standard direct integration method for background estimation [41]. It is possible for  
678 gamma rays from DM annihilation to scatter in transit to HAWC via Inverse Compton Scattering  
679 (ICS). This was investigated and its impact on the flux is basically zero. Supporting information  
680 on this is in Section 7.6.1

681 **7.3 Analysis**

682 The expected differential photon flux from DM-DM annihilation to standard model particles,  
683  $d\Phi_\gamma/dE_\gamma$ , over some solid angle, *Omega* is described by the familiar equation.

$$\frac{d\Phi_\gamma}{dE_\gamma} = \frac{\langle\sigma v\rangle}{8\pi m_\chi^2} \frac{dN_\gamma}{dE_\gamma} \times \int_{\text{source}} d\Omega \int_{l.o.s} dl \rho_\chi^2(r, \theta') \quad (7.1)$$

684 Where  $\langle\sigma v\rangle$  is the velocity weighted annihilation cross-section.  $\frac{dN}{dE}$  is the expected differential  
685 number of photons produced at each energy per annihilation.  $m_\chi$  is the rest mass of the supposed  
686 DM particle.  $J$  is the astrophysical J-factor and is defined as

$$J = \int d\Omega \int_{l.o.s} dl \rho_\chi^2(r, \theta') \quad (7.2)$$

687 Where  $\rho_\chi$  is the DM density.  $l$  is the distance to the source from Earth.  $r$  is the radial distance  
688 from the center of the source.  $\theta'$  is the half angle defining a cone containing the DM source. How  
689 each component is synthesized and considered for HAWC's analysis is presented in the following  
690 sections.

691 **7.3.1  $\frac{dN_\gamma}{dE_\gamma}$  - Particle Physics Component**

692 For these spectra, we import the PPPC with Electroweak (EW) corrections [43]. The spectrum  
693 is implemented as a model script in astromodels for 3ML. The EW corrections were previously not  
694 considered for HAWC and are significant for DM annihilating to EW coupled SM particles such  
695 as all leptons, and the  $\gamma$ ,  $Z$ , and  $W$  bosons [45]. Figure 7.2 demonstrates the significance of EW  
696 corrections for W boson annihilation. Across EW SM channels, the gamma-ray spectra become  
697 harder than spectra without EW corrections. Tables from the PPPC were reformatted into Python  
698 NumPy dictionaries for collaboration-wide use. A class in astromodels was developed to include  
699 the EW correction from the PPPC and is aptly named `PPPCSpectra` within `DM_models.py`.

700 **7.3.2  $J$ - Astrophysical Component**

701 The J-factor profiles for each source are imported from Geringer-Sameth (referred to with  $\mathcal{GS}$ )  
702 [44]. These were pulled from the publication as  $J(\theta)$ , where  $\theta$  is the angular separation from the  
703 center of the source. HAWC requires maps in terms of  $\frac{dJ}{d\Omega}$ , so the conversion from the maps was  
704 done in the following way...

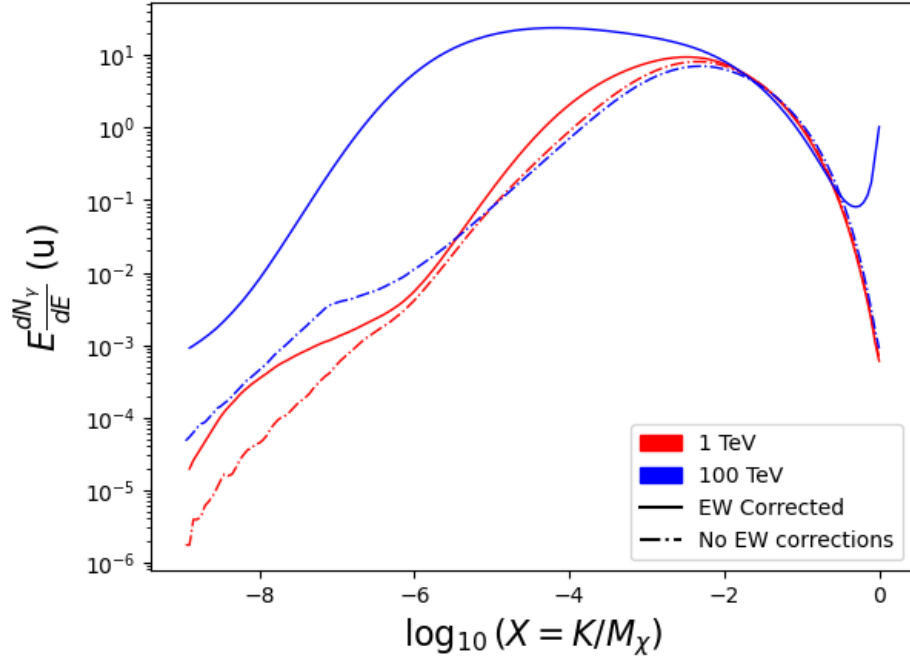


Figure 7.2 Effect of Electro-Weak (EW) corrections on expected DM annihilation spectrum for  $\chi\chi \rightarrow W^-W^+$ . Solid lines are spectral models that consider EW corrections. Dash-dot lines are spectral models without EW corrections. Red lines are models for  $M_\chi = 1$  TeV. Blue lines represent models for  $M_\chi = 100$  TeV. All models are sourced from the PPPC4DMID [43].

705 First, convert the angular distances to solid angles

$$\Omega = 2 \cdot \pi(1 - \cos(\theta)) \quad (7.3)$$

706 which reduces with a small angle approximation to  $\pi\theta^2$ . Next, the central difference for both the  $\Delta J$   
707 and  $\Delta\Omega$  value were calculated for the discretized form of  $J(\theta)$  with the central difference stencil:

$$\Delta\phi_i = \phi_{i+1} - \phi_{i-1} \quad (7.4)$$

708 Where  $\phi$  is either  $\Omega$  or  $J$ . These were done separately in case the grid spacing in  $\theta$  was not uniform.

709 Finally, these lists are divided so that we are left with an approximation of the  $dJ/d\Omega$  profile that  
710 is a function of  $\theta$ . Admittedly, this is an approximation method for the map which introduces small  
711 errors compared to the true profile estimate. This was checked as a systematic against the author's  
712 profiling of the spatial distribution and is documented in Section 7.7.1.

713 With  $\frac{dJ}{d\Omega}(\theta)$ , a map is generated, first by filling in the north-east quadrant of the map. This  
714 quadrant is then reflected twice, vertically then horizontally, to fill the full map. Maps are then

715 normalized by dividing the discrete 2D integral of the map. The 2D integral was a simple height  
716 of bins, Newton's integral:

$$p^2 \cdot \sum_{i,j=0}^{N,M} \frac{dJ}{d\Omega}(\theta_{i,j}) \quad (7.5)$$

717 These maps are HEALpix maps with NSIDE 16384 and saved in the `.fits` format.

718 Another DM spatial distribution model from Bonnivard ( $\mathcal{B}$ ) [46] was used for the Glory Duck  
719 study. However, to save computational time, limits from  $\mathcal{GS}$  were scaled to  $\mathcal{B}$  instead of each  
720 experiment performing a full study a second time. How these models compare is demonstrated for  
721 each dSph in Figure 7.15 and Figure 7.16. Plots of these maps are provided for each source in the  
722 sandbox directory: `GD_mass_profiles`. Examples of the two most impactful dSphs, Segue1 and  
723 Coma Berenices are featured in Figure 7.3

### 724 7.3.3 Source Selection and Annihilation Channels

725 We use many of the dSph presented in our previous dSph DM search [45]. HAWC's sources  
726 for Glory Duck include Boötes I, Coma Berenices, Canes Venatici I + II, Draco, Hercules, Leo I,  
727 II, + IV, Segue 1, Sextans, and Ursa Major I + II. A full description of all sources used in Glory  
728 Duck is found in Table 7.1. Triangulum II was excluded from the Glory Duck analysis because  
729 of large uncertainties in its J-factor. Ursa Minor was excluded from HAWC's contribution to the  
730 combination because the source extension model extended Ursa Minor beyond HAWC's field of  
731 view. Ursa Minor was not expected to contribute significantly to the combined limit, so work was  
732 not invested in a solution to include Ursa Minor.

733 The DM annihilation channels probed for the Glory Duck combination include  $b\bar{b}$ ,  $e\bar{e}$ ,  $\mu\bar{\mu}$ ,  $\tau\bar{\tau}$ ,  
734  $t\bar{t}$ ,  $W^+W^-$ , and  $ZZ$ . A summary of all sources, with a description of each experiments' sensitivity  
735 to the source, is provided in Table 7.2.

### 736 7.3.4 Likelihood Methods

737 We perform a standard HAWC binned maximum likelihood analysis using  $f_{hit}$  bins 1-9. This  
738 analysis was performed using HAL and 3ML, in Python2 [41, 42]. With these tools we compute  
739 the max from the likelihood profiles and perform a ratio test to calculate the significance of each

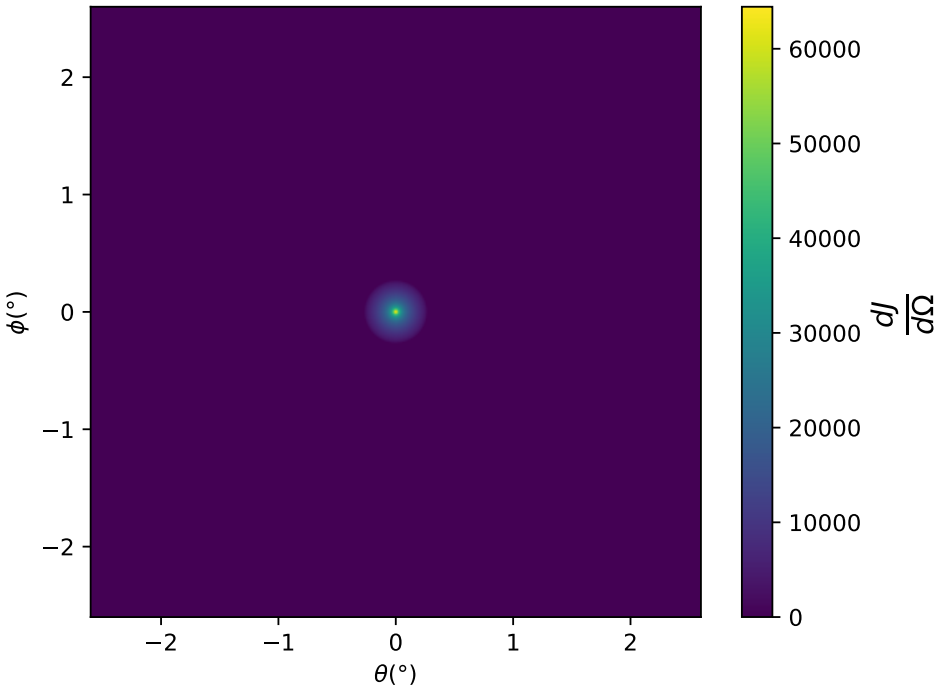
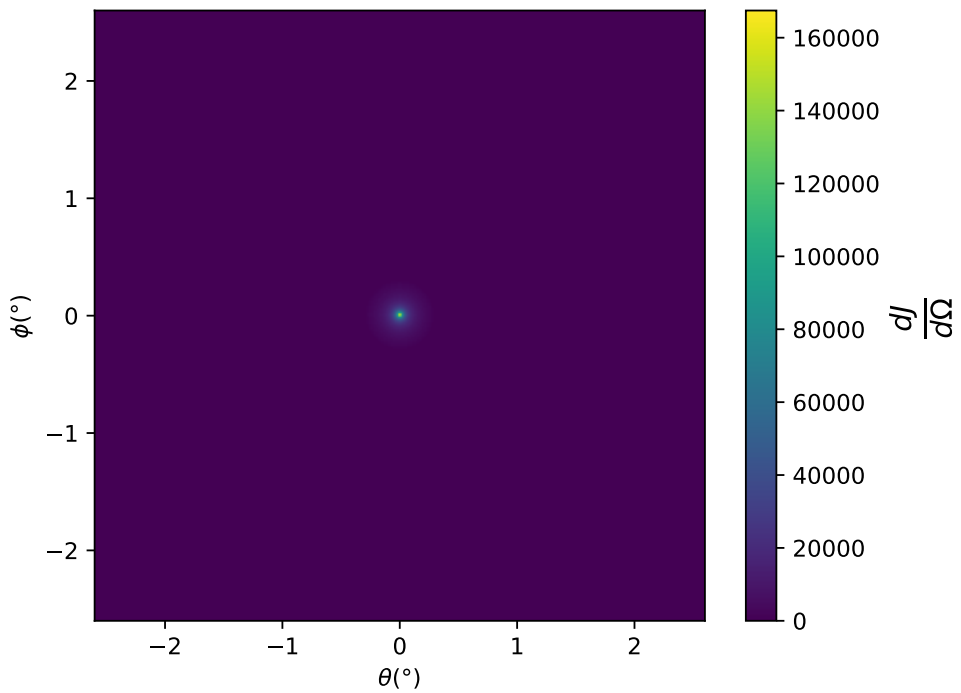


Figure 7.3  $\frac{dJ}{d\Omega}$  maps for Segue1 (top) and Coma Berenices (bottom). Origin is centered on the specific dwarf spheroidal galaxies (dSph). X and Y axes are the angular separation from the center of the dwarf. Plots of the remaining 11 dSph HAWC studied are linked in [TODO: cref to appendix](#).

Table 7.1 Summary of the relevant properties of the dSphs used in the present work. Column 1 lists the dSphs. Columns 2 and 3 present their heliocentric distance and galactic coordinates, respectively. Columns 4 and 5 report the  $J$ -factors of each source given from the  $\mathcal{GS}$  and  $\mathcal{B}$  independent studies and their estimated  $\pm 1\sigma$  uncertainties. The values  $\log_{10} J$  ( $\mathcal{GS}$  set) [44] correspond to the mean  $J$ -factor values for a source extension truncated at the outermost observed star. The values  $\log_{10} J$  ( $\mathcal{B}$  set) [46] are provided for a source extension at the tidal radius of each dSph. **Bolded sources are within HAWC's field of view and provided to the Glory Duck analysis.**

Name	Distance (kpc)	$l, b$ ( $^{\circ}$ )	$\log_{10} J$ ( $\mathcal{GS}$ set) $\log_{10}(\text{GeV}^2\text{cm}^{-5}\text{sr})$	$\log_{10} J$ ( $\mathcal{B}$ set) $\log_{10}(\text{GeV}^2\text{cm}^{-5}\text{sr})$
<b>Boötes I</b>	66	358.08, 69.62	$18.24^{+0.40}_{-0.37}$	$18.85^{+1.10}_{-0.61}$
<b>Canes Venatici I</b>	218	74.31, 79.82	$17.44^{+0.37}_{-0.28}$	$17.63^{+0.50}_{-0.20}$
<b>Canes Venatici II</b>	160	113.58, 82.70	$17.65^{+0.45}_{-0.43}$	$18.67^{+1.54}_{-0.97}$
Carina	105	260.11, -22.22	$17.92^{+0.19}_{-0.11}$	$18.02^{+0.36}_{-0.15}$
<b>Coma Berenices</b>	44	241.89, 83.61	$19.02^{+0.37}_{-0.41}$	$20.13^{+1.56}_{-1.08}$
<b>Draco</b>	76	86.37, 34.72	$19.05^{+0.22}_{-0.21}$	$19.42^{+0.92}_{-0.47}$
Fornax	147	237.10, -65.65	$17.84^{+0.11}_{-0.06}$	$17.85^{+0.11}_{-0.08}$
<b>Hercules</b>	132	28.73, 36.87	$16.86^{+0.74}_{-0.68}$	$17.70^{+1.08}_{-0.73}$
<b>Leo I</b>	254	225.99, 49.11	$17.84^{+0.20}_{-0.16}$	$17.93^{+0.65}_{-0.25}$
<b>Leo II</b>	233	220.17, 67.23	$17.97^{+0.20}_{-0.18}$	$18.11^{+0.71}_{-0.25}$
<b>Leo IV</b>	154	265.44, 56.51	$16.32^{+1.06}_{-1.70}$	$16.36^{+1.44}_{-1.65}$
Leo V	178	261.86, 58.54	$16.37^{+0.94}_{-0.87}$	$16.30^{+1.33}_{-1.16}$
Leo T	417	214.85, 43.66	$17.11^{+0.44}_{-0.39}$	$17.67^{+1.01}_{-0.56}$
Sculptor	86	287.53, -83.16	$18.57^{+0.07}_{-0.05}$	$18.63^{+0.14}_{-0.08}$
<b>Segue I</b>	23	220.48, 50.43	$19.36^{+0.32}_{-0.35}$	$17.52^{+2.54}_{-2.65}$
Segue II	35	149.43, -38.14	$16.21^{+1.06}_{-0.98}$	$19.50^{+1.82}_{-1.48}$
<b>Sextans</b>	86	243.50, 42.27	$17.92^{+0.35}_{-0.29}$	$18.04^{+0.50}_{-0.28}$
<b>Ursa Major I</b>	97	159.43, 54.41	$17.87^{+0.56}_{-0.33}$	$18.84^{+0.97}_{-0.43}$
<b>Ursa Major II</b>	32	152.46, 37.44	$19.42^{+0.44}_{-0.42}$	$20.60^{+1.46}_{-0.95}$
Ursa Minor	76	104.97, 44.80	$18.95^{+0.26}_{-0.18}$	$19.08^{+0.21}_{-0.13}$

Table 7.2 Summary of dSph observations by each experiment used in this work. A ‘-’ indicates the experiment did not observe the dSph for this study. For Fermi-LAT, the exposure at 1 GeV is given. For HAWC,  $|\Delta\theta|$  is the absolute difference between the source declination and HAWC latitude. HAWC is more sensitive to sources with smaller  $|\Delta\theta|$ . For IACTs, we show the zenith angle range, the total exposure, the energy range, the angular radius  $\theta$  of the signal or ON region, the ratio of exposures between the background-control (OFF) and signal (ON) regions ( $\tau$ ), and the significance of gamma-ray excess in standard deviations,  $\sigma$ .

Source name	Fermi-LAT	HAWC	H.E.S.S, MAGIC, VERITAS						
	Exposure ( $10^{11}$ s m $^2$ )	$ \Delta\theta $ ( $^\circ$ )	IACT	Zenith ( $^\circ$ )	Exposure (h)	Energy range (GeV)	$\theta$ ( $^\circ$ )	$\tau$	$S$ ( $\sigma$ )
Boötes I	2.6	4.5	VERITAS	15 – 30	14.0	100–41000	0.10	8.6	-1.0
Canes Venatici I	2.9	14.6	–	–	–	–	–	–	–
Canes Venatici II	2.9	15.3	–	–	–	–	–	–	–
Carina	3.1	–	H.E.S.S.	27 – 46	23.7	310 – 70000	0.10	18.0	-0.3
Coma Berenices	2.7	4.9	H.E.S.S.	47 – 49	11.4	550 – 70000	0.10	14.4	-0.4
			MAGIC	5 – 37	49.5	60 – 10000	0.17	1.0	–
			MAGIC	29 – 45	52.1	70 – 10000	0.22	1.0	–
Draco	3.8	38.1	VERITAS	25 – 40	49.8	120 – 70000	0.10	9.0	-1.0
Fornax	2.7	–	H.E.S.S.	11 – 25	6.8	230 – 70000	0.10	45.5	-1.5
Hercules	2.8	6.3	–	–	–	–	–	–	–
Leo I	2.5	6.7	–	–	–	–	–	–	–
Leo II	2.6	3.1	–	–	–	–	–	–	–
Leo IV	2.4	19.5	–	–	–	–	–	–	–
Leo V	2.4	–	–	–	–	–	–	–	–
Leo T	2.6	–	–	–	–	–	–	–	–
Sculptor	2.7	–	H.E.S.S.	10 – 46	11.8	200 – 70000	0.10	19.8	-2.2
Segue I	2.5	2.9	MAGIC	13 – 37	158.0	60 – 10000	0.12	1.0	-0.5
			VERITAS	15 – 35	92.0	80 – 50000	0.10	7.6	0.7
Segue II	2.7	–	–	–	–	–	–	–	–
Sextans	2.4	20.6	–	–	–	–	–	–	–
Ursa Major I	3.4	32.9	–	–	–	–	–	–	–
Ursa Major II	4.0	44.1	MAGIC	35 – 45	94.8	120 – 10000	0.30	1.0	-2.1
Ursa Minor	4.1	–	VERITAS	35 – 45	60.4	160 – 93000	0.10	8.4	-0.1

source. This analysis is identical to the previous dSph analysis [45] except the sources are treated as extended. For the vast majority of our sources, this extension is no greater than 2 degrees. We calculate the likelihood of each source and model, assuming events are Poisson distributed, with

$$\mathcal{L} = \prod_i \frac{(B_i + S_i)^{N_i} e^{-(B_i + S_i)}}{N_i!} \quad (7.6)$$

$S_i$  is the sum of expected number of signal counts.  $B_i$  is the number of background counts observed.  $N_i$  is the total number of counts. The  $i$ th bin is iterated over spatial and  $f_{\text{hit}}$ . Then we combine the profiles across all five experiments. The profile likelihood ratio  $\lambda$  as a function of annihilation cross-section  $\langle\sigma v\rangle$  is computed by:

$$\lambda(\langle\sigma v\rangle | \mathcal{D}_{\text{dSphs}}) = \frac{\mathcal{L}(\langle\sigma v\rangle; \hat{\nu} | \mathcal{D}_{\text{dSphs}})}{\mathcal{L}(\widehat{\langle\sigma v\rangle}; \hat{\nu} | \mathcal{D}_{\text{dSphs}})} \quad (7.7)$$

for a considered annihilation channel and DM mass.

**TODO: Section pasted from paper. Rephrase cause plagiarism is a thing.** As mentioned previously, each experiment computes the  $\mathcal{L}_{lk}$  from Equation (7.7) differently. The remainder of this section highlights the differences in this calculation across the experiments. Four experiments, namely *Fermi*-LAT, H.E.S.S., HAWC and MAGIC, use a binned likelihood to compute the  $\mathcal{L}_{lk}$ . For these experiments, for each observation  $\mathcal{D}_{lk}$  of a given dSph  $l$  carried out using a given gamma-ray detector  $k$ , the binned likelihood function is:

$$\mathcal{L}_{lk}(\langle\sigma v\rangle; J_l, \nu_{lk} | \mathcal{D}_{lk}) = \prod_{i=1}^{N_E} \prod_{j=1}^{N_P} \left[ \mathcal{P}(s_{lk,ij}(\langle\sigma v\rangle, J_l, \nu_{lk}) + b_{lk,ij}(\nu_{lk}) | N_{lk,ij}) \right] \times \mathcal{L}_{lk,\nu}(\nu_{lk} | \mathcal{D}_{\nu_{lk}}) \quad (7.8)$$

where  $N_E$  and  $N_P$  are the number of considered bins in reconstructed energy and arrival direction, respectively;  $\mathcal{P}$  represents a Poisson PDF for the number of gamma-ray candidate events observed in the  $i$ -th bin in energy and  $j$ -th bin in arrival direction, when the expected number is the sum of the expected mean number of signal events  $s_{ij}$  (produced by DM annihilation) and of background events  $b_{ij}$ ;  $\mathcal{L}_{lk,\nu}$  is the likelihood term for the extra  $\nu_{lk}$  nuisance parameters that vary from one instrument  $k$  to another. The expected counts for signal events  $s_{ij}$  for a given dSph  $l$  and detector  $k$  is given by:

$$s_{ij}(\langle\sigma v\rangle, J) = \int_{E'_{\min,i}}^{E'_{\max,i}} dE' \int_{P'_{\min,j}}^{P'_{\max,j}} d\Omega' \int_0^\infty dE \int_{\Delta\Omega_{tot}} d\Omega \int_0^{T_{\text{obs}}} dt \frac{d^2\Phi(\langle\sigma v\rangle, J)}{dEd\Omega} \text{IRF}(E', P' | E, P, t) \quad (7.9)$$

762 where  $E'$  and  $E$  are the reconstructed and true energies,  $P'$  and  $P$  the reconstructed and true  
 763 arrival directions;  $E'_{\min,i}$ ,  $P'_{\min,j}$ ,  $E'_{\max,i}$ , and  $P'_{\max,j}$  are their lower and upper limits of the  $i$ -th  
 764 energy bin and the  $j$ -th arrival direction bin;  $T_{\text{obs}}$  is the (dead-time corrected) total observation  
 765 time;  $t$  is the time along the observations;  $d^2\Phi/dEd\Omega$  is the DM flux in the source region (see  
 766 Equation (7.1)); and  $\text{IRF}(E', P' | E, P, t)$  is the IRF, which can be factorized as the product of the  
 767 effective collection area of the detector  $A_{\text{eff}}(E, P, t)$ , the PDFs for the energy estimator  $f_E(E' | E, t)$ ,  
 768 and arrival direction  $f_P(P' | E, P, t)$  estimators. Note that for Fermi-LAT, HAWC, MAGIC, and  
 769 VERITAS the effect of the finite angular resolution is taken into account through the convolution  
 770 of  $d\Phi/dEd\Omega$  with  $f_P$  in Equation (7.9), whereas in the cases of H.E.S.S.  $f_P$  is approximated by a  
 771 delta function. This approximation has been made in order to maintain compatibility of the result  
 772 with what has been previously published. The difference introduced by this approximation is  $< 5\%$   
 773 for all considered dSphs. **TODO: End of paper section**

774 From Equation (7.7), we can compute the test statistic (TS) with the ratio test:

$$\text{TS} = -2 \ln \left( \frac{\mathcal{L}}{\mathcal{L}^{\text{max}}} \right). \quad (7.10)$$

775  $\mathcal{L}^{\text{max}}$  here is equivalent to  $\mathcal{L}(N_i, B_i, S_i = 0)$  or no signal counts.

## 776 7.4 HAWC Results

777 13 of the 20 dSphs considered for the Glory Duck analysis are within HAWC's field of view.  
 778 These dSph are analyzed for emission from DM annihilation according to the likelihood method  
 779 described in Section 7.3.4. The 13 likelihood profiles are then combined to create a combined limit  
 780 on the dark matter cross-section. This combination is done for the 7 annihilation channels used in  
 781 the Glory Duck analysis. Figure 7.5 shows the combined limit for all annihilation channels with  
 782 HAWC only observations. We also perform 300 studies of Poisson trials on the background. These  
 783 trials are used to produce HAWC Brazil bands which were shared with the other collaborators for

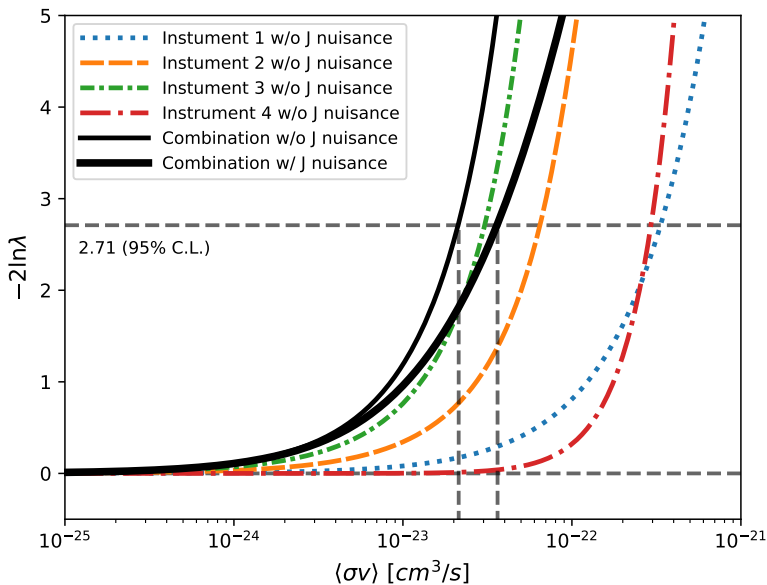


Figure 7.4 Illustration of the combination technique showing a comparison between  $-2 \ln \lambda$  provided by four instruments (colored lines) from the observation of the same dSph without any  $J$  nuisance and their sum, *i.e.* the resulting combined likelihood (thin black line). According to the test statistics of Equation (7.10), the intersection of the likelihood profiles with the line  $-2 \ln \lambda = 2.71$  indicates the 95% C.L. upper limit on  $\langle \sigma v \rangle$ . The combined likelihood (thin black line) shows a smaller value of upper limit on  $\langle \sigma v \rangle$  than those derived by individual instruments. We also show the uncertainties on the  $J$ -factor affects the combined likelihood and degrade the upper limit on  $\langle \sigma v \rangle$  (thick black line). All likelihood profiles are normalized so that the global minimum  $\widehat{\langle \sigma v \rangle}$  is 0. We note that each profile depends on the observational conditions in which a target object was observed. The sensitivity of a given instrument can be degraded and the upper limits less constraining if the observations are performed in non optimal conditions such as a high zenith angle or a short exposure time.

784 combined Brazil Bands. The results on fitting to HAWC's poisson trials of the DM hypothesis is  
 785 shown in Figure 7.6 for seven of the DM annihilation channels.

786 No DM was found in HAWC observations. The limits are dominated by the dSph Segue1 and  
 787 Coma Berenices. The remaining 11 dSphs do no contribute significantly to the limit. Even though  
 788 some of the remaining dSphs have large  $J$ -factors, they are towards the edge of HAWC's field of  
 789 view where this analysis is less sensitive.

## 790 7.5 Glory Duck Combined Results

791 The crux of this analysis is that HAWC's results are combined with 4 other gamma-ray obser-  
 792 vatories: Fermi-LAT, H.E.S.S., MAGIC, and VERITAS. The complete joint likelihood for the  $l$ -th

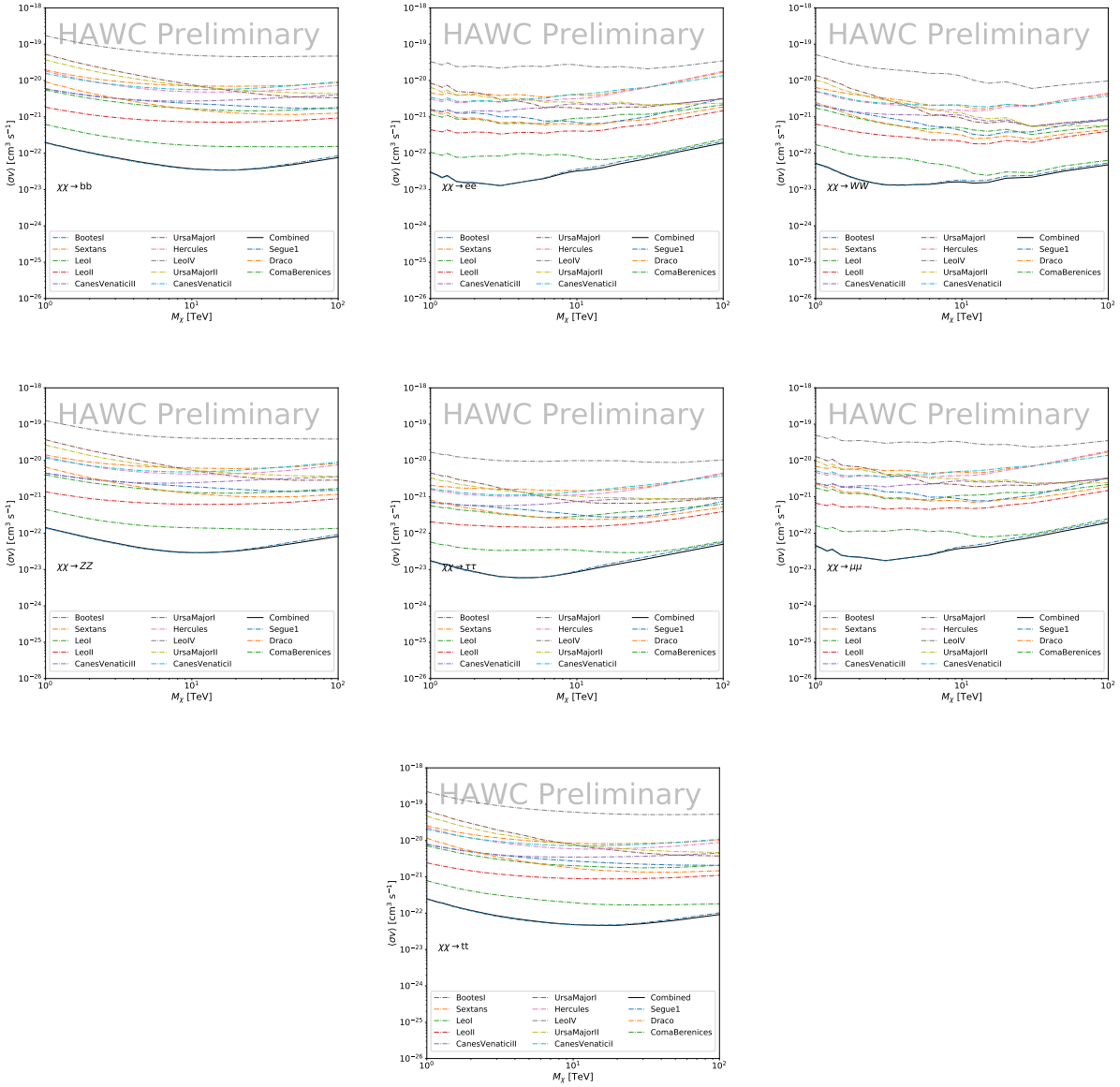


Figure 7.5 HAWC upper limits at 95% confidence level on  $\langle\sigma v\rangle$ versus DM mass for seven annihilation channels, using the set of  $J$ -factors from Ref. [47]. The solid line represents the observed combined limit. Dashed lines represent limits from individual dSphs.

793 dSph is the product of likelihood functions of the 5 experiments.

#### 794 TODO: place holder for results

795 The *partial* joint likelihood function for gamma-ray observations of each dSph ( $\mathcal{L}_{\text{dSph},l}$ ) is  
796 written as the product of the likelihood terms describing the  $N_{\text{exp},l}$  observations performed with

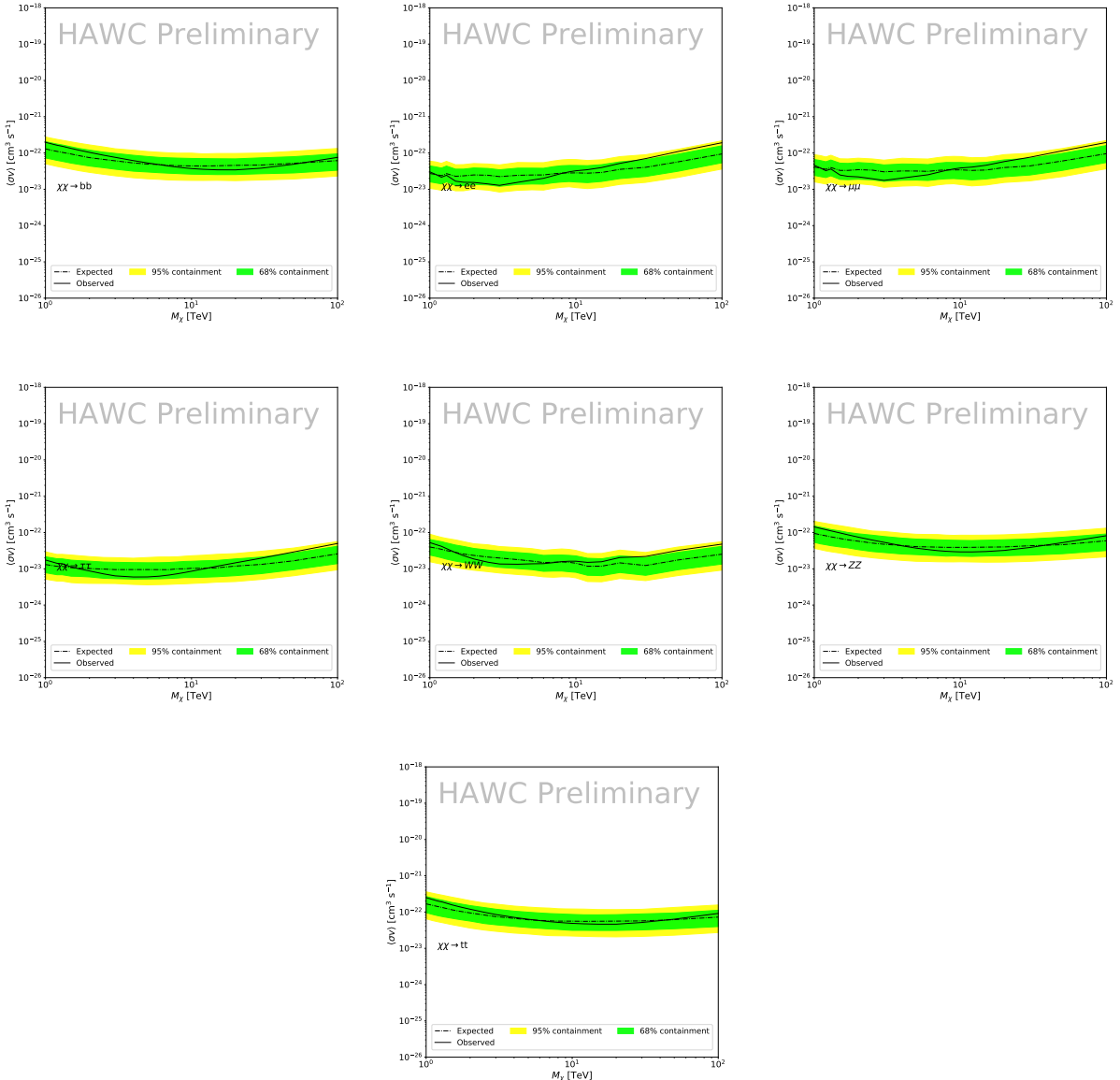


Figure 7.6 HAWC Brazil bands at 95% confidence level on  $\langle\sigma v\rangle$  versus DM mass for seven annihilation channels with  $J$ -factors from  $\mathcal{GS}$  [47]. The solid line represents the combined limit from 13 dSphs. The dashed line is the expected limit. The green band is the 68% containment. The yellow band is the 95% containment.

797 any of our observatories:

$$\mathcal{L}_{\text{dSph},l} (\langle\sigma v\rangle; J_l, \nu_l | \mathcal{D}_l) = \prod_{k=1}^{N_{\text{exp},l}} \mathcal{L}_{lk} (\langle\sigma v\rangle; J_l, \nu_{lk} | \mathcal{D}_{lk}), \quad (7.11)$$

798 where each  $\mathcal{L}_{lk}$  term refers to an observation of the  $l$ -th dSph with associated  $k$ -th instrument

799 responses.  $N_{\text{exp},l}$  varies from dSph to dSph and can be retrieved from Tab. 7.2.

800        Each collaboration separately analyses their data for  $\mathcal{D}_{lk}$  corresponding to dSph  $l$  and gamma-  
 801        ray detector  $k$ , using as many common assumptions as possible in the analysis (see the next  
 802        paragraph and further down in this section for additional details). No significant DM emission was  
 803        observed by any of the five telescopes. We present upper limits on  $\langle\sigma v\rangle$  using the test statistics,  
 804        Eq. (7.10).

$$TS = -2 \ln \lambda(\langle\sigma v\rangle), \quad (7.12)$$

805        No significant DM emission was observed by any of the five instruments. We present the upper  
 806        limits on  $\langle\sigma v\rangle$  assuming seven independent DM self annihilation channels, namely  $W^+W^-$ ,  $Z^+Z^-$ ,  
 807         $b\bar{b}$ ,  $t\bar{t}$ ,  $e^+e^-$ ,  $\mu^+\mu^-$ , and  $\tau^+\tau^-$ . The 68% and 95% containment bands are produced from 300  
 808        Poisson realizations of the null hypothesis corresponding to each of the combined datasets. These  
 809        300 realizations are combined identically to dSph observations. The containment bands and the  
 810        median are extracted from the distribution of resulting limits on the null hypothesis. These 300  
 811        realizations are obtained either by fast simulations of the OFF observations, for H.E.S.S., MAGIC,  
 812        VERITAS, and HAWC, or taken from real observations of empty fields of view in the case of  
 813        Fermi-LAT [48, 49, 50].

814        The obtained limits are shown in Figure 7.7 for the  $\mathcal{GS}$  set of  $J$ -factors [47] and in Figure 7.8  
 815        for the  $\mathcal{B}$  set of  $J$ -factors [46, 51]. The combined limits are presented with their 68% and 95%  
 816        containment bands, and are expected to be close to the median limit when no signal is present.  
 817        We observe agreement with the null hypothesis for all channels, within  $2\sigma$  standard deviations,  
 818        between the observed limits and the expectations given by the median limits. Limits obtained from  
 819        each detector are also indicated in the figures, where limits for all dSphs observed by the specific  
 820        instrument have been combined.

821        Below  $\sim 300$  GeV, the *Fermi*-LAT dominates the DM limits for all annihilation channels. From  
 822         $\sim 300$  GeV to  $\sim 2$  TeV, *Fermi*-LAT continues to dominate for the hadronic and bosonic DM channels,  
 823        yet the IACTs (H.E.S.S., MAGIC, and VERITAS) and *Fermi*-LAT all contribute to the limit for  
 824        leptonic DM channels. For DM masses between  $\sim 2$  TeV to  $\sim 10$  TeV, the IACTs dominate leptonic

825 DM annihilation channels, whereas both the *Fermi*-LAT and the IACTs dominate bosonic and  
826 hadronic DM annihilation channels. From  $\sim 10$  TeV to  $\sim 100$  TeV, both the IACTs and HAWC  
827 contribute significantly to the leptonic DM limit. For hadronic and bosonic DM, the IACTs and  
828 *Fermi*-LAT both contribute strongly.

829 We notice that the limits computed using the  $\mathcal{B}$  set of  $J$ -factor are always better compared to the  
830 ones calculated with the  $\mathcal{GS}$  set. For the  $W^+W^-$ ,  $Z^+Z^-$ ,  $b\bar{b}$ , and  $t\bar{t}$  channels, the ratio between the  
831 limits computed with the two sets of  $J$ -factor is varying between a factor of  $\sim 3$  and  $\sim 5$  depending  
832 on the energy, with the largest ratio around 10 TeV. For the channels  $e^+e^-$ ,  $\mu^+\mu^-$ , and  $\tau^+\tau^-$ , the  
833 ratio lies between  $\sim 2$  to  $\sim 6$ , being maximum around 1 TeV. Examining Figure 7.15 and Figure 7.16  
834 in Section 7.7, these differences are explained by the fact that the  $\mathcal{B}$  set provides higher  $J$ -factors  
835 for the majority of the studied dSphs, with the notable exception of Segue I. The variation on the  
836 ratio of the limits for the two sets is due to different dSph dominating the limits depending on the  
837 energy. This pushes the range of thermal cross-section which can be excluded to higher mass. This  
838 comparison demonstrates the magnitude of systematic uncertainties associated with the choice of  
839 the  $J$ -factor

840 This comparison demonstrates the magnitude of systematic uncertainties associated with the  
841 choice of the  $J$ -factor calculation. The  $\mathcal{GS}$  and  $\mathcal{B}$  sets present a difference in the limits for all  
842 channels of about This difference is explained, see Figure 7.15 and Figure 7.16 in Appendix, by the  
843 fact that the  $\mathcal{B}$  set provides higher  $J$  factors for all dSph except for Segue I. This pushes the range  
844 of thermal cross-section which can be excluded to higher mass.

## 845 7.6 HAWC Systematics

### 846 7.6.1 Inverse Compton Scattering

847 The DM-DM annihilation channels produce many high energy electrons regardless of the  
848 primary annihilation channel. These high energy electrons can produce high energy gamma-rays  
849 through Inverse Compton Scattering (ICS). If this effect is strong, it would change the morphology  
850 of the source and increase the total expected gamma-ray counts from any source. The PPPC [43]  
851 provides tools in Mathematica for calculating the impact of ICS for an arbitrary location in the

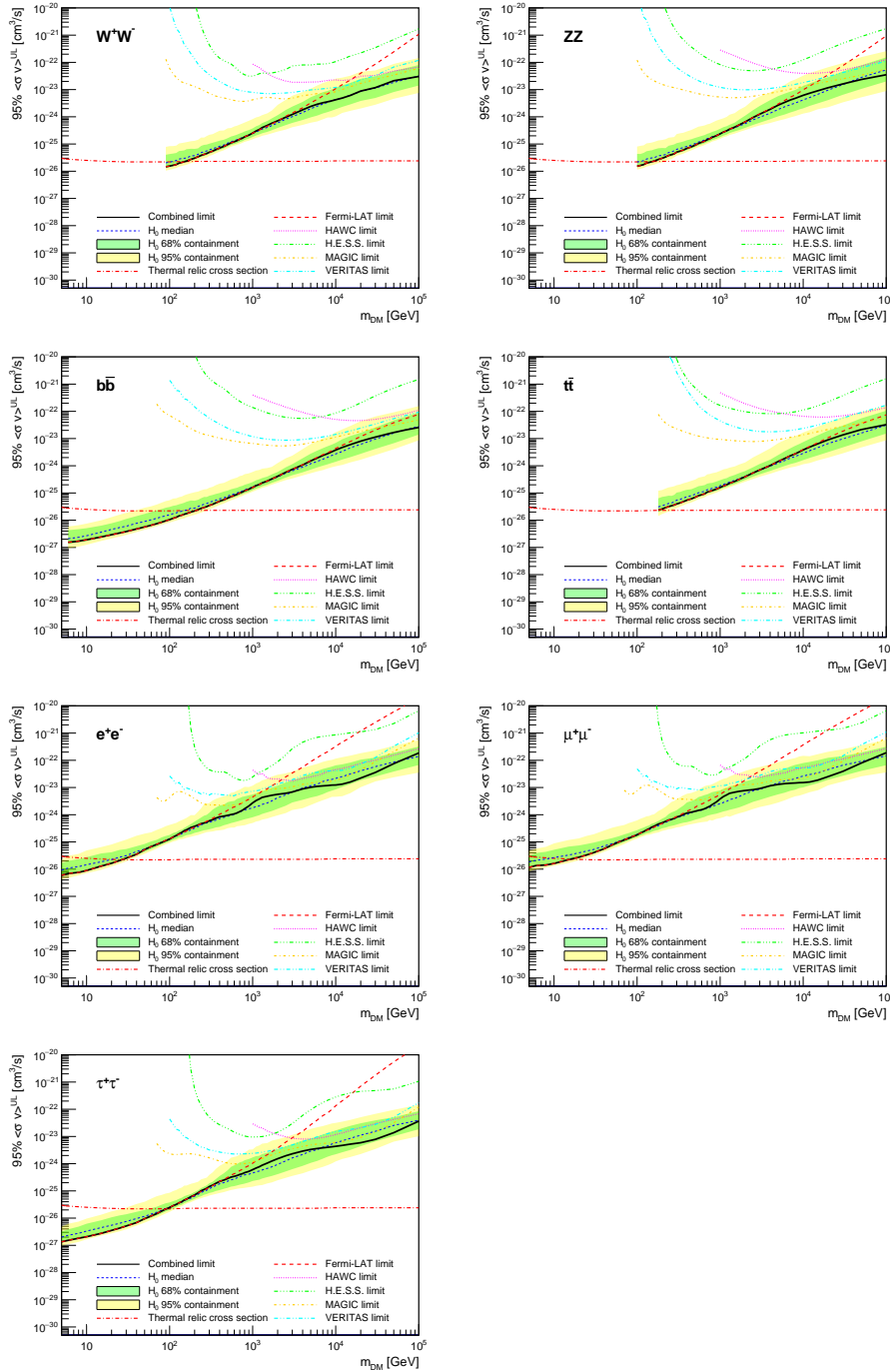


Figure 7.7 Upper limits at 95% confidence level on  $\langle\sigma v\rangle$  in function of the DM mass for eight annihilation channels, using the set of  $J$  factors from Ref. [47] ( $\mathcal{GS}$  set in Table 7.1). The black solid line represents the observed combined limit, the black dashed line is the median of the null hypothesis corresponding to the expected limit, while the green and yellow bands show the 68% and 95% containment bands. Combined upper limits for each individual detector are also indicated as solid, colored lines. The value of the thermal relic cross-section in function of the DM mass is given as the red dotted-dashed line [52].

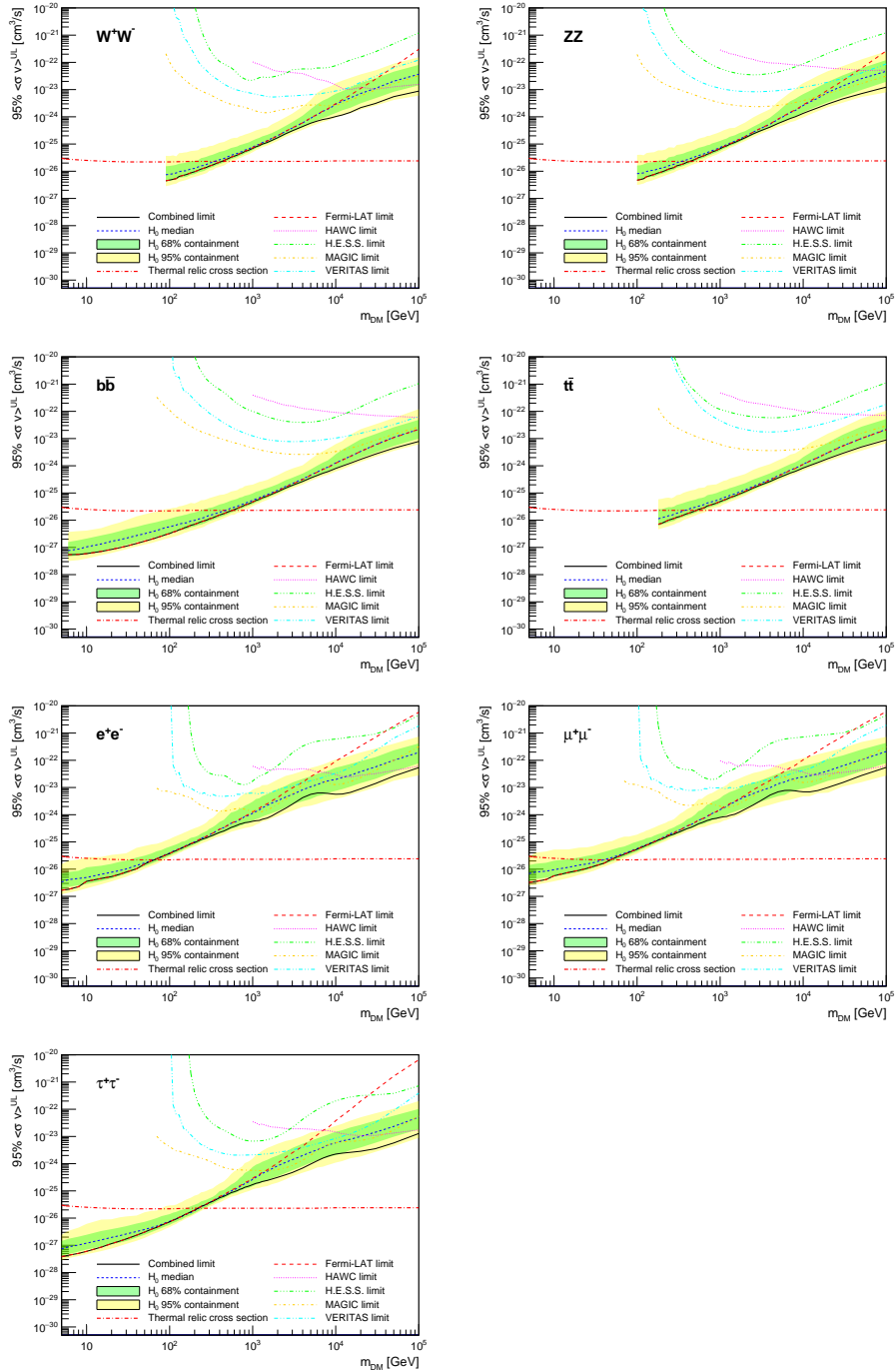


Figure 7.8 Same as Fig. 7.7, using the set of  $J$  factors from Ref. [46, 51] ( $\mathcal{B}$  set in Table 7.1).

sky for a specified annihilation channel. We calculated the change in gamma-ray counts for DM annihilation to primary  $e\bar{e}$  for RA and Dec corresponding to Segue1 and Coma Berenices. These dSphs were chosen because they are the strongest contributors to the limit.  $e\bar{e}$  was selected because it would have the largest number of high energy electrons. The effect was found to be on the order

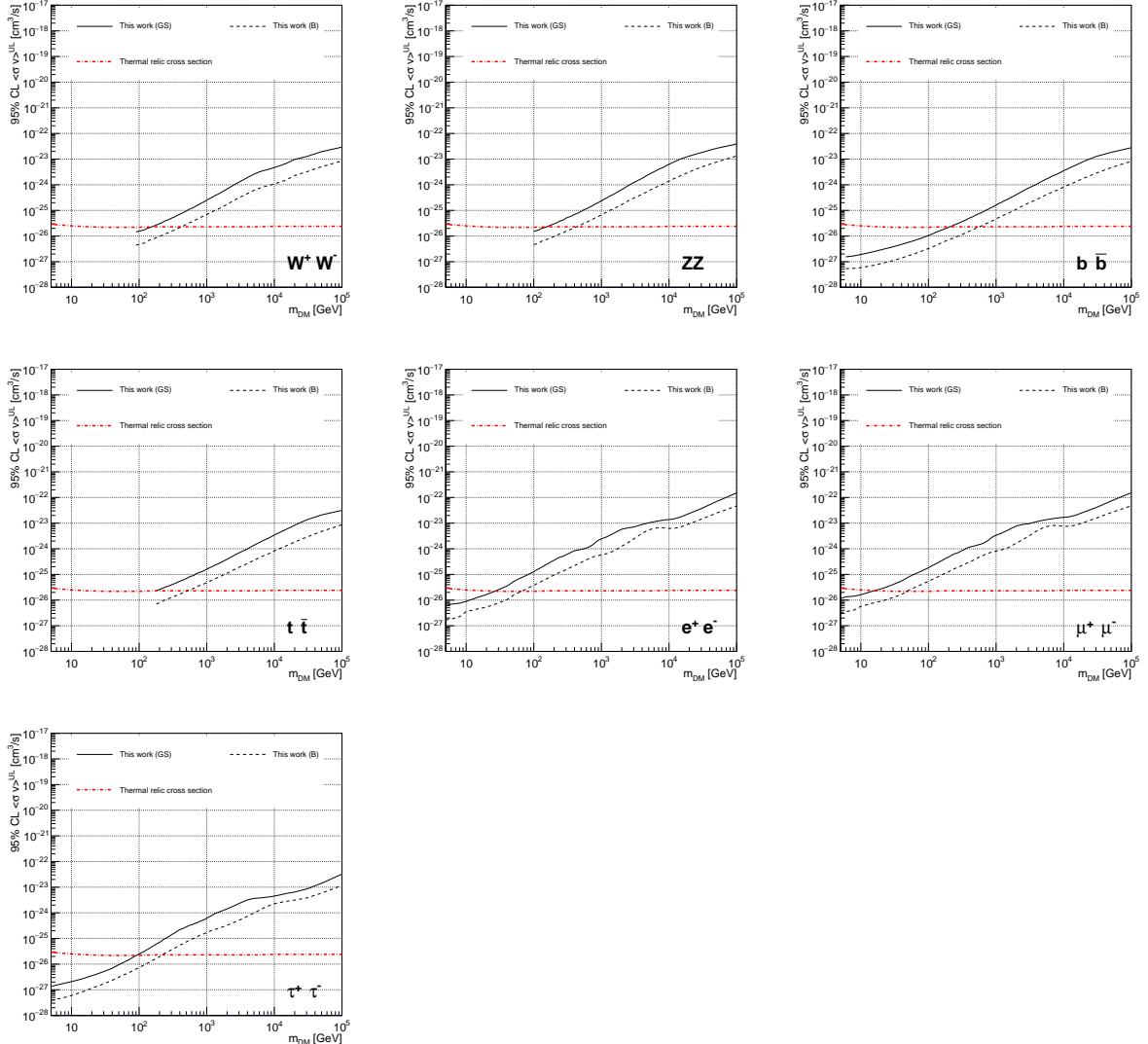


Figure 7.9 Comparisons of the combined limits at 95% confidence level for each of the eight annihilation channels when using the  $J$  factors from Ref. [47] ( $\mathcal{GS}$  set in Table 7.1), plain lines, and the  $J$  factor from Ref. [46, 51] ( $\mathcal{B}$  set in Table 7.1), dashed lines. The cross-section given by the thermal relic is also indicated [52].

856 of  $10^{-7}$  on the gamma-ray spectrum. As a result, this systematic is not considered in our analysis.

## 857 7.6.2 Point Source Versus Extended Source Limits

858 The previous DM search toward dSph approximated the dSphs as point sources [45]. In  
 859 this analysis, the dSphs are implemented as extended with J-factor distributions following those  
 860 produced by [47]. The resolution of the cited map is much finer than HAWC's angular resolution.  
 861 The vast majority of the J-factor distribution is represented on the central HAWC pixel of the dSph

862 spatial map. However, the neighboring 8 pixels are not negligible and contribute to our limit.

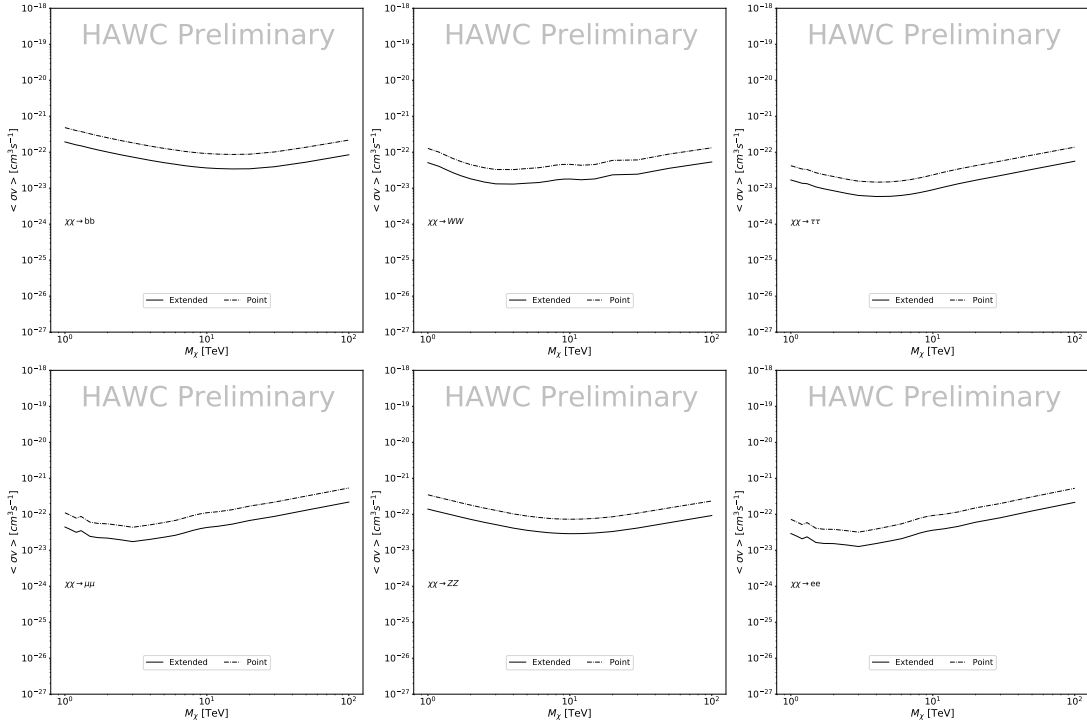


Figure 7.10 Comparisons of the combined limits at 95% confidence level for a point source analysis and extended source using [47]  $\mathcal{GS}$  J-factor distributions and PPPC [43] annihilation spectra. Shown are the limits for Segue1 which will have the most significant impact on the combined limit. 6 of the 7 DM annihilation channels are shown. Solid lines are extended source studies. Dashed lines are point source studies. Overall, the extended source analysis improves the limit by a factor of 2.

863     Figure 7.10 shows a substantial improvement to the limit for Segue1. Fig. 7.11 however showed  
 864 identical limits. These disparities are best explained by the relative difference in their J-Factors.  
 865 Both dSphs pass almost overhead the HAWC detector, however Segue1 has the larger J-Factor  
 866 between the two. Adjacent pixels to the central pixel will therefore contribute to the limits. This is  
 867 the case for other dSph that are closer to overhead the HAWC detector.

868     Comparison plots for all sources and the combined limit can be found in the sandbox for the  
 869 Glory Duck project.

### 870 7.6.3 Impact of Pointing Systematic

871     During the analysis it was discovered that reconstruction of gamma-rays. Slides describing this  
 872 systematic can be found [here](#). Shown on the presentation is dependence on the pointing systematic

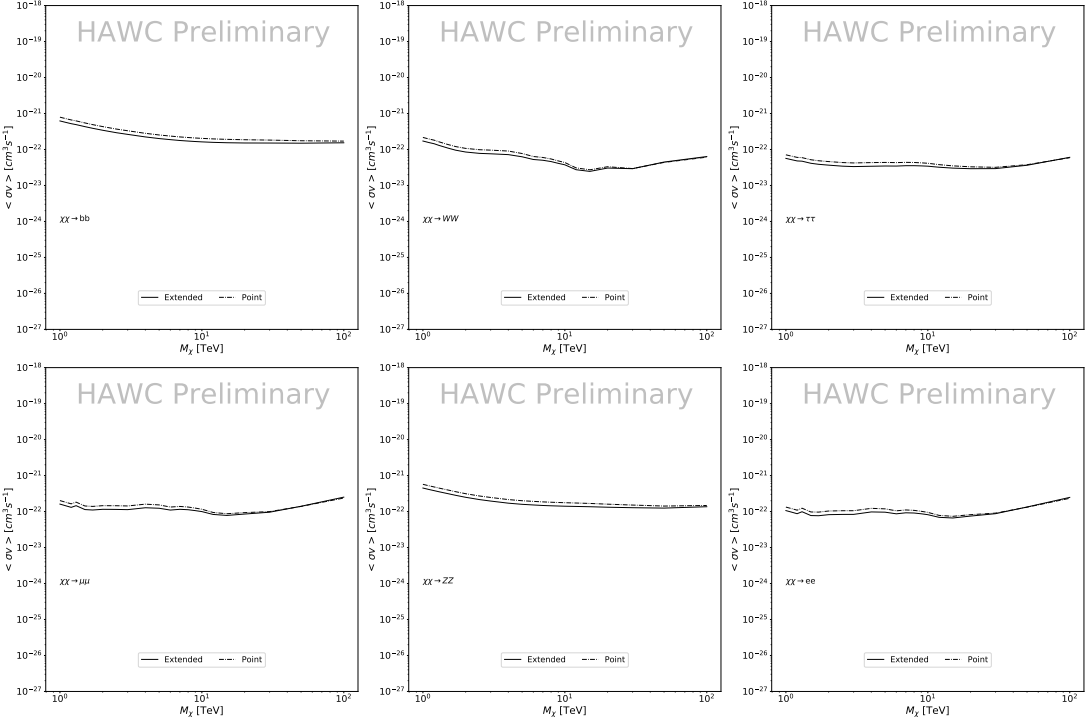


Figure 7.11 Same as Fig. 7.10 on Coma Berenices. This dSph also contributes significantly to the limit. The limits are identical in this case.

873 on declination. New spatial profiles were generated for every dSph and limits were computed for  
 874 the adjusted declination.

875 Section 7.6.3 demonstrates the impact of this systematic for all DM annihilation channels  
 876 studied by HAWC. The impact is a tiny improvement, yet mostly identical, to the combined limits.

## 877 7.7 J-factor distributions

### 878 7.7.1 Numerical integration of $\mathcal{GS}$ maps

879 It was discovered well after the HAWC analysis was completed that the published tables from  
 880  $\mathcal{GS}$  [44] quoted median  $J$ -factors were computed in a non-trivial manner. The assumption myself  
 881 and collaborators had was that the published tables represented the  $J$ -factor as a function of  $\theta$  for  
 882 the best global fit model on a per source basis. However, this is not the case. Instead, what is  
 883 published are the best fit model for each dwarf that only considers stars up to the angular separation  
 884  $\theta$ . Therefore, the model is changing for each value of  $\theta$  for each dwarf. Yet, the introduced features  
 885 from unique models at each  $\theta$  are much smaller than the angular resolution of HAWC. It is not

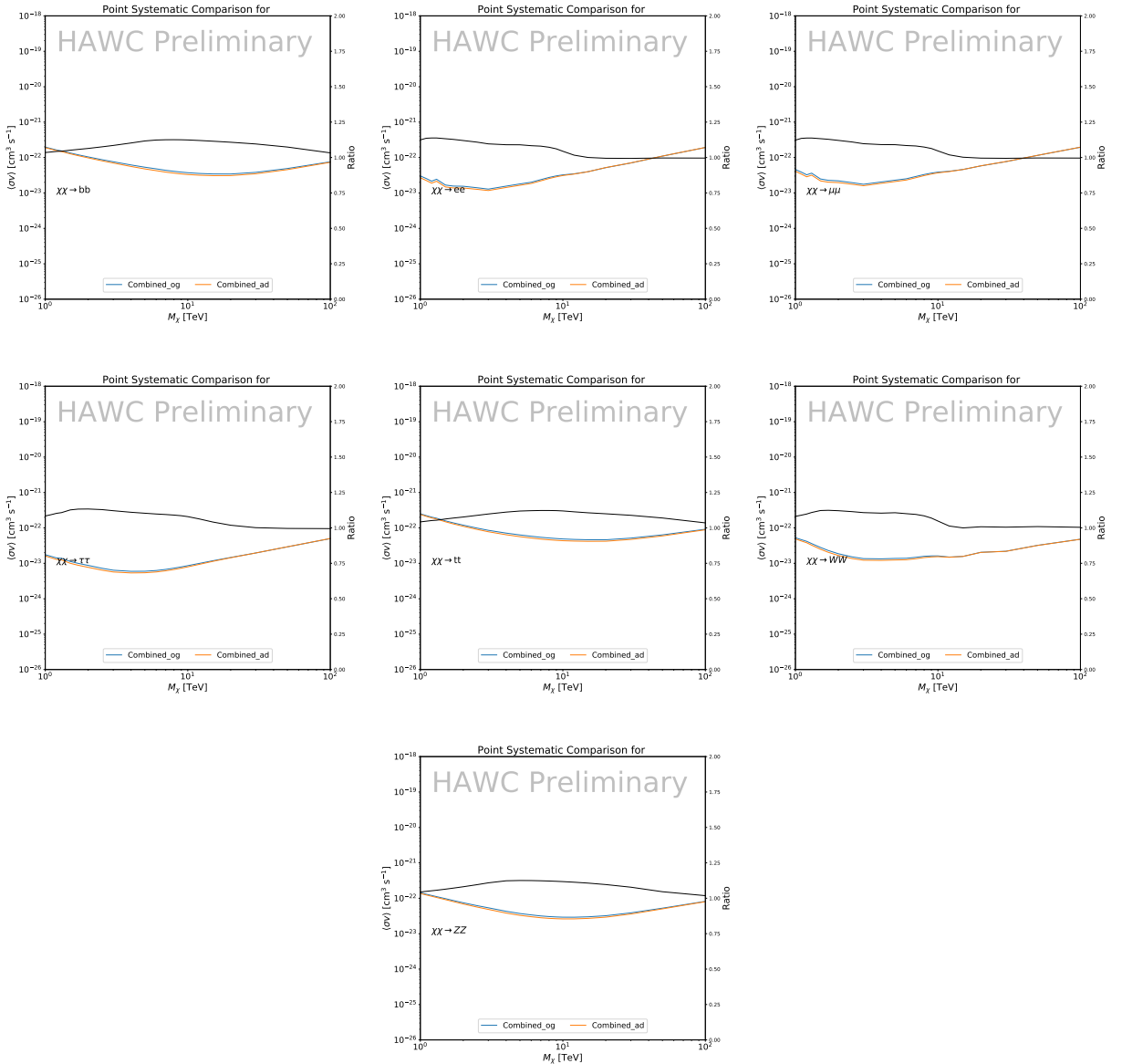


Figure 7.12 Comparison of combined limits when correcting for HAWC's pointing systematic. All DM annihilation channels are shown. The solid black line is the ratio between published limit to the declination corrected limit. The blue solid line or "Combined\_og" represented the limits computed for Glory Duck. The solid orange line or "Combined\_ad" represented the limits computed after correcting for the pointing systematic.

886 expected for these effects to impact the limits and TS greatly as a result.  
887 Median  $J$ -factor model profiles were provided by the authors. New maps were generated  
888 and analyzed for Segue1 and Coma Berenices. Figure 7.13 shows the differential between maps  
889 generated with the method from Section 7.7.1 and from the authors of [44]. These maps were

890 reanalyzed for all SM DM annihilation channels. Upper limits for these channels are shown in  
891 Figure 7.14

892 From Figure 7.14, we can see that the impact of these model difference was no substantial.  
893 The observed impact was a fractional effect which is much smaller than the impact from selecting  
894 another DM spatial distribution model as was shown in Figure 7.9.

### 895 7.7.2 $\mathcal{GS}$ versus $\mathcal{B}$ spatial models

896 We show in this appendix a comparison between the  $J$ -factors computed by Geringer-Sameth  
897 *et al.* [47] (the  $\mathcal{GS}$  set) and the ones computed by Bonnivard *et al.* [46, 51] (the  $\mathcal{B}$  set). The  
898  $\mathcal{GS}$   $J$ -factors are computed through a Jeans analysis of the kinematic stellar data of the selected  
899 dSphs, assuming a dynamic equilibrium and a spherical symmetry for the dSphs. They adopted  
900 the generalized DM density distribution, known as Zhao-Hernquist, introduced by [53], carrying  
901 three additional index parameters to describe the inner and outer slopes, and the break of the  
902 density profile. Such a profile parametrization allows the reduction of the theoretical bias from  
903 the choice of a specific radial dependency on the kinematic data. In other words, the increase of  
904 free parameters with the use of the Zhao-Hernquist profile allows a better description of the mass  
905 density distribution of dark matter.

906 In addition, a constant velocity anisotropy profile and a Plummer light profile [54] for the stellar  
907 distribution were assumed. The velocity anisotropy profile depends on the radial and tangential  
908 velocity dispersions. However, its determination remains challenging since only the line-of-sight  
909 velocity dispersion can be derived from velocity measurements. Therefore, the parametrization of  
910 the anisotropy profile is obtained from simulated halos (see [55] for more details). They provide the  
911 values of the  $J$ -factors of regions extending to various angular radius up to the outermost member  
912 star.

913 The  $\mathcal{B}$   $J$ -factors were computed through a Jeans analysis taking into account the systematic  
914 uncertainties induced by the DM profile parametrization, the radial velocity anisotropy profile, and  
915 the triaxiality of the halo of the dwarf galaxies. They performed a more complete study of the dSph  
916 kinematics and dynamics than  $\mathcal{GS}$  for the determination of the  $J$ -factor. Conservative values of the

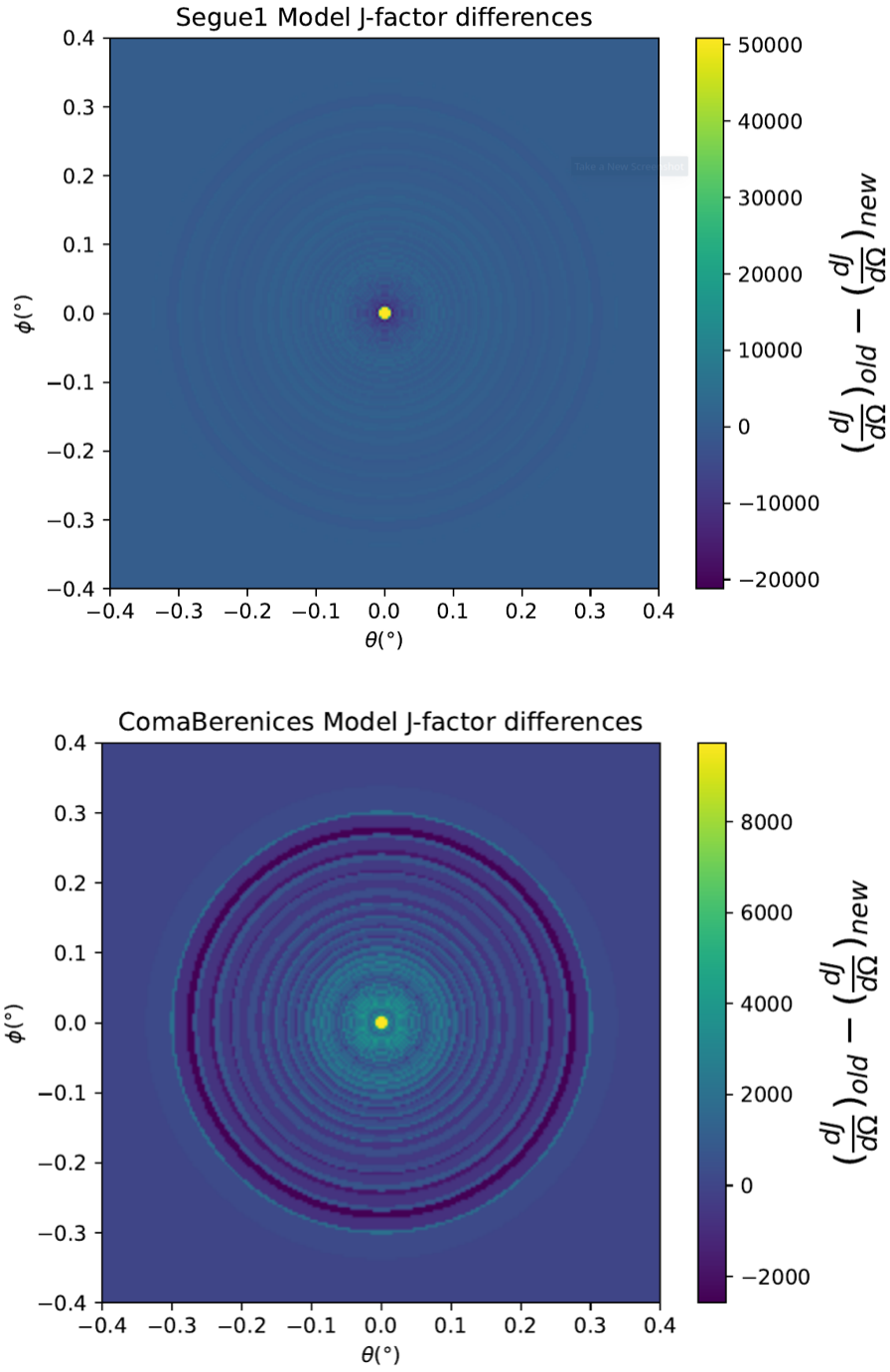


Figure 7.13 Differential map of  $dJ/\Omega$  from model built in Section 7.7.1 and profiles provided directly from authors. (Top) Differential from Segue1. (bottom) Differential from Coma Berenices. Note that their scales are not the same. Segue1 shows the deepest discrepancies which is congruent with its large uncertainties. Both models show anuli where unique models become apparent.

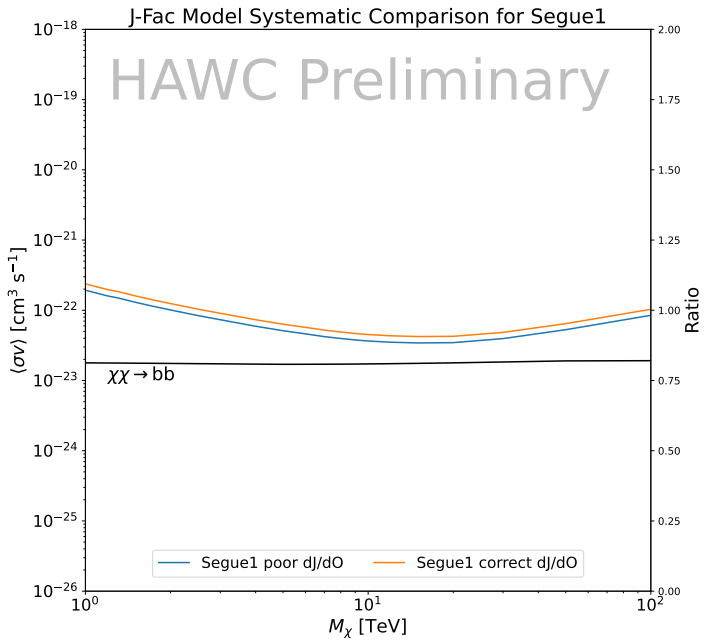
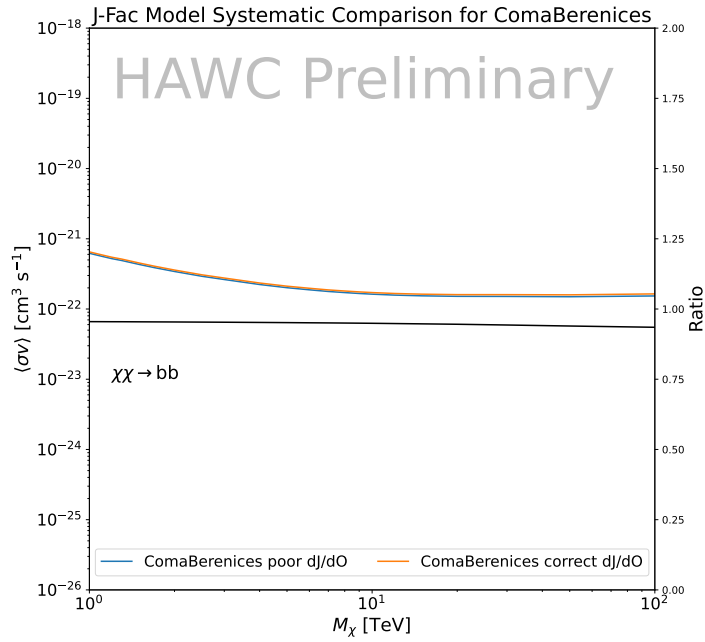


Figure 7.14 HAWC limits for Coma Berenices (top) and Segue1 (bottom) for two different map sets. Blue lines are limits calculated on maps with poor model representation. Orange lines are limits calculated on spatial profiles provided by the authors of [44]. Black line is the ratio of the poor spatial model limits to the corrected spatial models. The left y-axis measures  $\langle \sigma v \rangle$  for the blue and orange lines. The right y-axis measures the ratio and is unitless.

917  $J$ -factors where obtained using an Einasto DM density profile [56], a realistic anisotropy profile  
918 known as the Baes & Van Hese profile [57] which takes into account that the inner regions can be  
919 significantly non-isotropic, and a Zhao-Hernquist light profile [53].

920 For both sets,  $J$ -factor values are provided for all dSphs as a function of the radius of the  
921 integration region [47, 46, 51]. Table 7.1 shows the heliocentric distance and Galactic coordinates  
922 of the twenty dSphs, together with the two sets of  $J$ -factor values integrated up to the outermost  
923 observed star for  $\mathcal{GS}$  and the tidal radius for  $\mathcal{B}$ . Both  $J$ -factor sets were derived through a Jeans  
924 analysis based on the same kinematic data, except for Draco where the measurements of [58] have  
925 been adopted in the computation of the  $\mathcal{B}$  value. The computations for producing the  $\mathcal{GS}$  and  $\mathcal{B}$   
926 samples differ in the choice of the DM density, velocity anisotropy, and light profiles, for which the  
927 set  $\mathcal{B}$  takes into account some sources of systematic uncertainties.

928 Figure 7.15 and Figure 7.16 show the comparisons for the  $J$ -factor versus the angular radius  
929 for each of the 20 dSphs used in this study. The uncertainties provided by the authors are also  
930 indicated in the figures. For the  $\mathcal{GS}$  set, the computation stops at the angular radius corresponding  
931 to the outermost observed star, while for the  $\mathcal{B}$  set, the computation stops at the angular radius  
932 corresponding to the tidal radius.

## 933 7.8 Discussion and Conclusions

934 In this multi-instrument analysis, we have used observations of 20 dSphs from the gamma-ray  
935 telescopes Fermi-LAT, H.E.S.S., MAGIC, VERITAS, and HAWC to perform a collective DM  
936 search annihilation signals. The data were combined across sources and detectors to significantly  
937 increase the sensitivity of the search. We have observed no significant deviation from the null, no  
938 DM, hypothesis, and so present our results in terms of upper limits on the annihilation cross section  
939 for seven potential DM annihilation channels.

940 Fermi-LAT brings the most stringent constraints for continuum channels below approximately  
941 1 TeV. the remaining detectors dominate at higher energies. Overall, for multi-TeV DM mass,  
942 the combined DM constraints from all five telescopes are 2-3 times stronger than any individual  
943 telescope for multi-TeV DM.

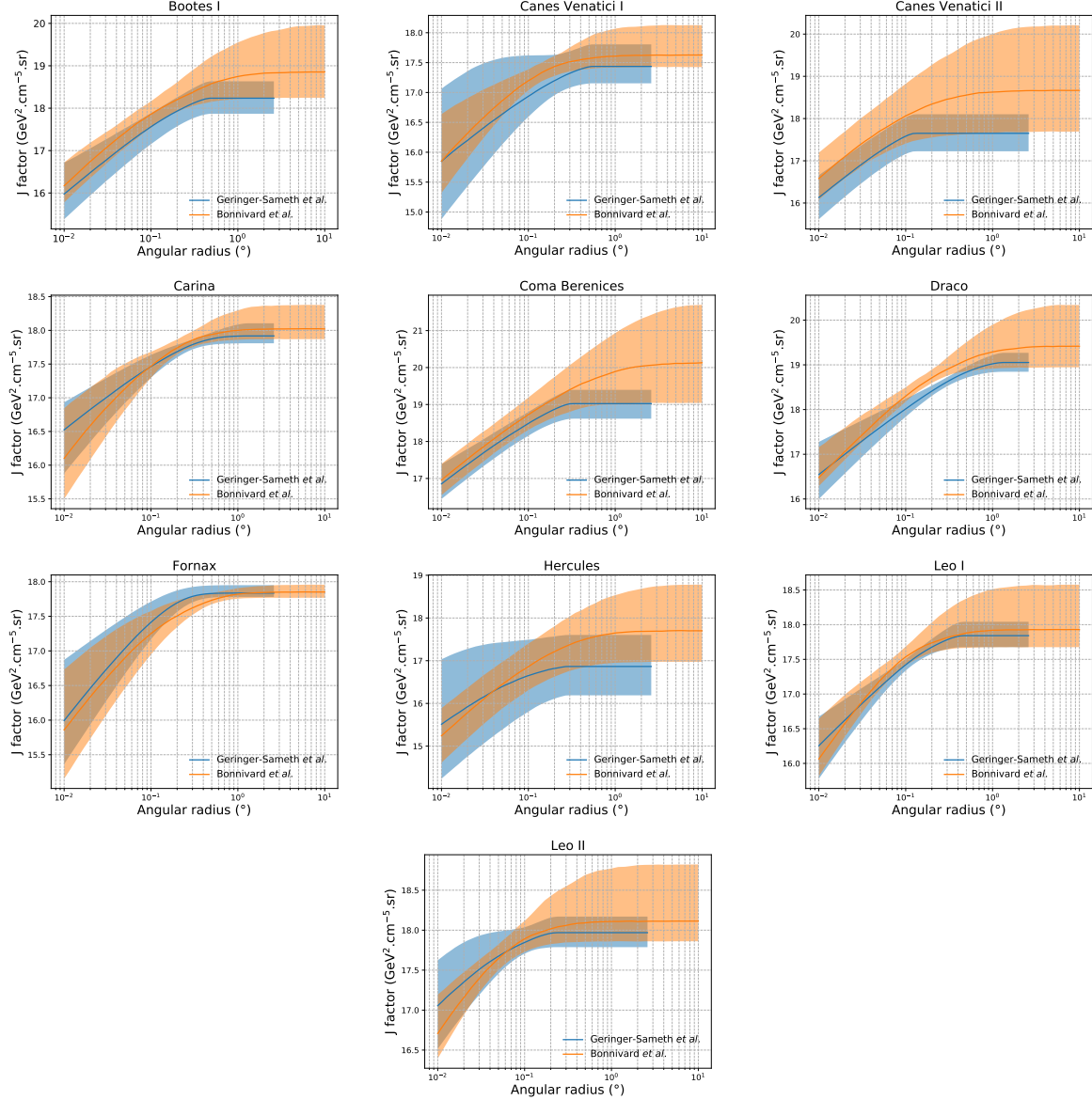


Figure 7.15 Comparisons between the  $J$ -factors versus the angular radius for the computation of  $J$  factors from Ref. [47] ( $\mathcal{GS}$  set in Table 7.1) in blue and for the computation from Ref. [46, 51] ( $\mathcal{B}$  set in Tab. 7.1) in orange. The solid lines represent the central value of the  $J$ -factors while the shaded regions correspond to the  $1\sigma$  standard deviation.

944 Derived from observations of many dSphs, our results produce robust limits given the DM  
 945 content of the dSphs is relatively well constrained. The obtained limits span the largest mass  
 946 range of any WIMP DM search. Our combined analysis improves the sensitivity over previously  
 947 published results from each detectors which produces the most stringent limits on DM annihilation  
 948 from dSphs. These results are based on deep exposures of the most promising known dSphs with

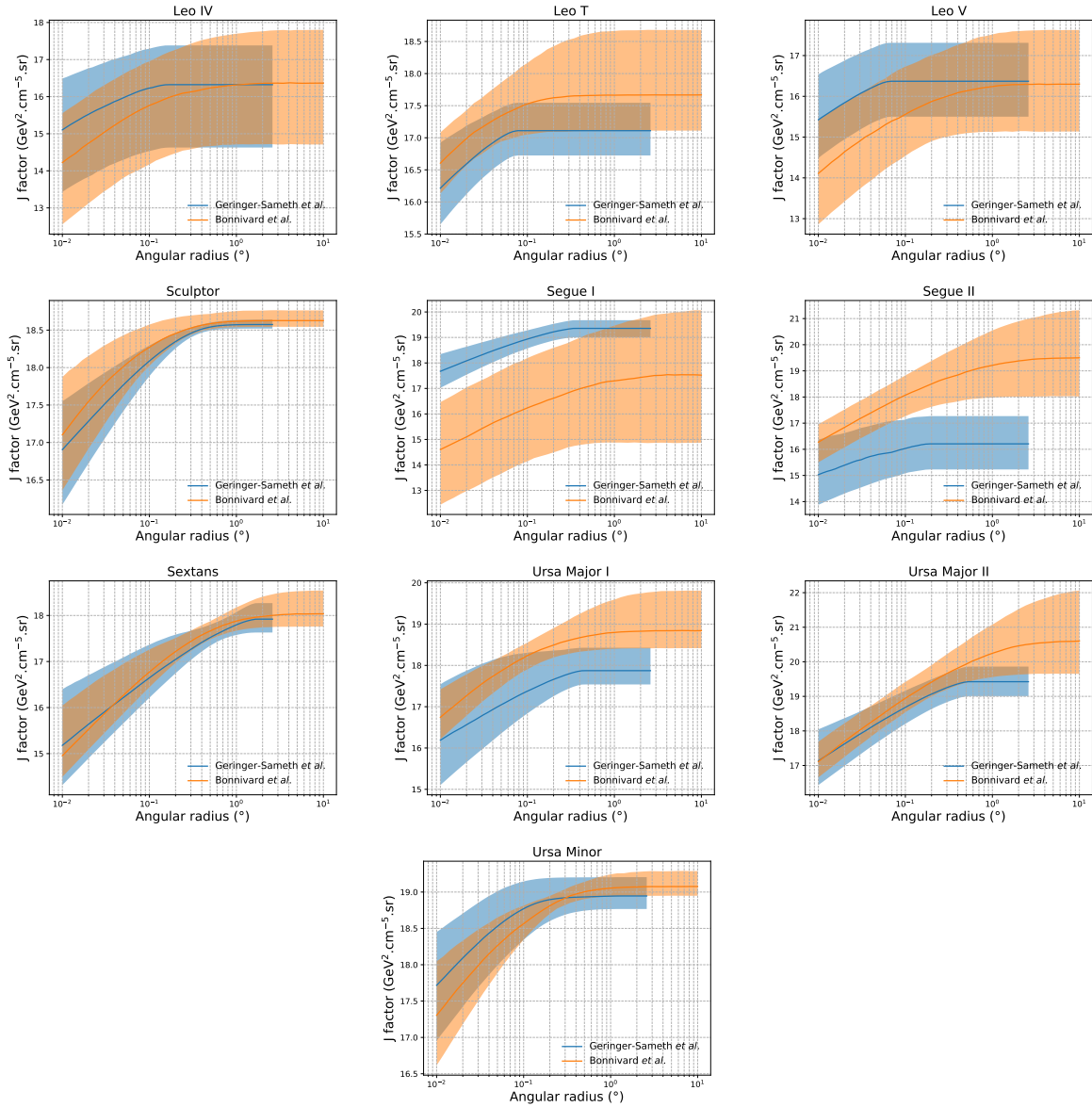


Figure 7.16 Comparisons between the  $J$ -factors versus the angular radius for the computation of  $J$  factors from Ref. [47] ( $\mathcal{GS}$  set in Tab. 7.1) in blue and for the computation from Ref. [46, 51] ( $\mathcal{B}$  set in Tab. 7.1) in orange. The solid lines represent the central value of the  $J$ -factors while the shaded regions correspond to the  $1\sigma$  standard deviation.

949 the currently most sensitive gamma-ray instruments. Therefore, our results constitute a legacy of  
 950 a generation of gamma-ray instruments on WIMP DM searches towards dSphs. Our results will  
 951 remain the reference in the field until a new generation of more sensitive gamma-ray instruments  
 952 begin operations, or until new dSphs with higher  $J$ -factors are discovered.

953 This analysis serves as a proof of concept for future multi-instrument and multi-messenger

954 combination analyses. With this collaborative effort, we have managed to sample over four orders  
955 in magnitude in gamma-ray energies with distinct observational techniques. Determining the nature  
956 of DM continues to be an elusive and difficult problem. Larger datasets with diverse measurement  
957 techniques could be essential to tackling the DM problem. A future collaboration using similar  
958 techniques as the ones described in this paper could grow even beyond gamma rays. The models we  
959 used for this study include annihilation channels with neutrinos in the final state. Advanced studies  
960 could aim to merge our results with those from neutrino observatories with large data sets. Efforts  
961 are already underway to add data from the IceCube, ANTARES, and KM3NeT observatories to  
962 these gamma-ray results.

963 From this work, a selection of the best candidates for observations, according to the latest  
964 knowledge on stellar dynamics and modelling techniques for the derivation of the  $J$ -factors on the  
965 potential dSphs targets, is highly desirable at the time that new experiments are starting their dark  
966 matter programmes using dSphs. Given the systematic uncertainty inherent to the derivation of  
967 the  $J$ -factors, an informed observational strategy would be to select both objects with the highest  
968  $J$ -factors that could lead to DM signal detection, and objects with robust  $J$ -factor predictions, i.e.  
969 with kinematic measurements on many bright stars, which would strengthen the DM interpretation  
970 reliability of the observation outcome.

971 This analysis combines data from multiple telescopes to produce strong constraints on astro-  
972 physical objects. From this perspective, these methods can be applied beyond just DM searches.  
973 Almost every astrophysical study can benefit from multi-telescope, multi-wavelength gamma-ray  
974 studies. We have enabled these telescopes to study the cosmos with greater precision and detail.  
975 Many astrophysical searches can benefit from multi-instrument gamma-ray studies, for which our  
976 analysis lays the foundation.

## **CHAPTER 8**

### **NU DUCK**

977

## CHAPTER 9

### MULTITHREADING HAWC ANALYSES FOR DARK MATTER SEARCHES

**APPENDIX****FIRST APPENDIX**

## BIBLIOGRAPHY

- 981 [1] Anne M. Green. “Dark matter in astrophysics/cosmology”. In: *SciPost Phys. Lect.*  
 982 *Notes* (2022), p. 37. doi: [10.21468/SciPostPhysLectNotes.37](https://doi.org/10.21468/SciPostPhysLectNotes.37). URL: <https://scipost.org/10.21468/SciPostPhysLectNotes.37>.
- 984 [2] Bing-Lin Young. “A survey of dark matter and related topics in cosmology”. In: *Frontiers*  
 985 *of Physics* 12 (Oct. 2016). doi: <https://doi.org/10.1007/s11467-016-0583-4>.  
 986 URL: <https://doi.org/10.1007/s11467-016-0583-4>.
- 987 [3] Gianfranco Bertone, Dan Hooper, and Joseph Silk. “Particle dark matter: evidence,  
 988 candidates and constraints”. In: *Physics Reports* 405.5 (2005), pp. 279–390. ISSN:  
 989 0370-1573. doi: <https://doi.org/10.1016/j.physrep.2004.08.031>. URL:  
 990 <https://www.sciencedirect.com/science/article/pii/S0370157304003515>.
- 991 [4] Gianfranco Bertone and Dan Hooper. “History of dark matter”. In: *Rev. Mod. Phys.*  
 992 90 (4 Aug. 2018), p. 045002. doi: [10.1103/RevModPhys.90.045002](https://doi.org/10.1103/RevModPhys.90.045002). URL: <https://link.aps.org/doi/10.1103/RevModPhys.90.045002>.
- 994 [5] Fritz Zwicky. “The Redshift of Extragalactic Nebulae”. In: *Helvetica Physica Acta* 6.  
 995 (1933), pp. 110–127. doi: [10.5169/seals-110267](https://doi.org/10.5169/seals-110267).
- 996 [6] Vera C. Rubin and Jr. Ford W. Kent. “Rotation of the Andromeda Nebula from a  
 997 Spectroscopic Survey of Emission Regions”. In: *ApJ* 159 (Feb. 1970), p. 379. doi:  
 998 [10.1086/150317](https://doi.org/10.1086/150317).
- 999 [7] K. G. Begeman, A. H. Broeils, and R. H. Sanders. “Extended rotation curves of spiral galax-  
 1000 ies: dark haloes and modified dynamics”. In: *Monthly Notices of the Royal Astronomical So-*  
 1001 *ciet* 249.3 (Apr. 1991), pp. 523–537. ISSN: 0035-8711. doi: [10.1093/mnras/249.3.523](https://doi.org/10.1093/mnras/249.3.523).  
 1002 eprint: <https://academic.oup.com/mnras/article-pdf/249/3/523/18160929/mnras249-0523.pdf>. URL: <https://doi.org/10.1093/mnras/249.3.523>.
- 1004 [8] *Different types of gravitational lenses*. website. Feb. 2004. URL: <https://esahubble.org/images/heic0404b/>.
- 1006 [9] Douglas Clowe et al. “A Direct Empirical Proof of the Existence of Dark Matter”. In: *apjl*  
 1007 648.2 (Sept. 2006), pp. L109–L113. doi: [10.1086/508162](https://doi.org/10.1086/508162). arXiv: [astro-ph/0608407](https://arxiv.org/abs/astro-ph/0608407)  
 1008 [*astro-ph*].
- 1009 [10] Planck Collaboration and N. et. al. Aghanim. “Planck 2018 results I. Overview and the  
 1010 cosmological legacy of Planck”. In: *A&A* 641 (2020). doi: [10.1051/0004-6361/201833880](https://doi.org/10.1051/0004-6361/201833880). URL: <https://doi.org/10.1051/0004-6361/201833880>.
- 1012 [11] Wayne Hu. *Matter Density Animation*. web. 2024. URL: <http://background.uchicago.edu/~whu/animbut/anim2.html>.

- 1014 [12] Wenlong Yuan et al. “A First Look at Cepheids in a Type Ia Supernova Host with JWST”. in:  
1015     *The Astrophysical Journal Letters* 940.1 (Nov. 2022). doi: [10.3847/2041-8213/ac9b27](https://doi.org/10.3847/2041-8213/ac9b27).  
1016     URL: <https://dx.doi.org/10.3847/2041-8213/ac9b27>.
- 1017 [13] Wendy L. Freedman. “Measurements of the Hubble Constant: Tensions in Perspective”. In:  
1018     *The Astrophysical Journal* 919.1 (Sept. 2021), p. 16. doi: [10.3847/1538-4357/ac0e95](https://doi.org/10.3847/1538-4357/ac0e95).  
1019     URL: <https://dx.doi.org/10.3847/1538-4357/ac0e95>.
- 1020 [14] Jodi Cooley. “Dark Matter direct detection of classical WIMPs”. In: *SciPost Phys. Lect.*  
1021     *Notes* (2022), p. 55. doi: [10.21468/SciPostPhysLectNotes.55](https://doi.org/10.21468/SciPostPhysLectNotes.55). URL: <https://scipost.org/10.21468/SciPostPhysLectNotes.55>.
- 1023 [15] “Search for new phenomena in events with an energetic jet and missing transverse momentum  
1024     in  $pp$  collisions at  $\sqrt{s} = 13$  TeV with the ATLAS detector”. In: *Phys. Rev. D* 103  
1025     (11 July 2021), p. 112006. doi: [10.1103/PhysRevD.103.112006](https://doi.org/10.1103/PhysRevD.103.112006). URL: <https://link.aps.org/doi/10.1103/PhysRevD.103.112006>.
- 1027 [16] *Jetting into the dark side: a precision search for dark matter*. website. July 2020. URL:  
1028     <https://atlas.cern/updates/briefing/precision-search-dark-matter>.
- 1029 [17] Celine Armand et. al. “Combined dark matter searches towards dwarf spheroidal galaxies  
1030     with Fermi-LAT, HAWC, H.E.S.S., MAGIC, and VERITAS”. in: *Proceedings of Science*.  
1031     Vol. 395. Mar. 2022. doi: <https://doi.org/10.22323/1.395.0528>.
- 1032 [18] Tracy R. Slatyer. “Les Houches Lectures on Indirect Detection of Dark Matter”. In: *SciPost*  
1033     *Phys. Lect. Notes* (2022), p. 53. doi: [10.21468/SciPostPhysLectNotes.53](https://doi.org/10.21468/SciPostPhysLectNotes.53). URL:  
1034     <https://scipost.org/10.21468/SciPostPhysLectNotes.53>.
- 1035 [19] Christian W Bauer, Nicholas L. Rodd, and Bryan R. Webber. “Dark matter spectra from  
1036     the electroweak to the Planck scale”. In: *Journal of High Energy Physics* 2021.1029-8479  
1037     (June 2021). doi: [https://doi.org/10.1007/JHEP06\(2021\)121](https://doi.org/10.1007/JHEP06(2021)121).
- 1038 [20] Riccardo Catena and Piero Ullio. “A novel determination of the local dark matter density”.  
1039     In: *Journal of Cosmology and Astroparticle Physics* 2010.08 (Aug. 2010), p. 004. doi:  
1040     [10.1088/1475-7516/2010/08/004](https://doi.org/10.1088/1475-7516/2010/08/004). URL: <https://dx.doi.org/10.1088/1475-7516/2010/08/004>.
- 1042 [21] B. P. Abbott et al. “Observation of Gravitational Waves from a Binary Black Hole Merger”.  
1043     In: *Phys. Rev. Lett.* 116 (6 Feb. 2016), p. 061102. doi: [10.1103/PhysRevLett.116.061102](https://doi.org/10.1103/PhysRevLett.116.061102). URL: <https://link.aps.org/doi/10.1103/PhysRevLett.116.061102>.
- 1045 [22] R. Abbasi et. al. “Observation of high-energy neutrinos from the Galactic plane”. In: *Science*  
1046     380.6652 (June 2023), pp. 1338–1343.
- 1047 [23] NASA Goddard Space Flight Center. *Fermi’s 12-year view of the gamma-ray sky*. website.

- 1048 2022. URL: <https://svs.gsfc.nasa.gov/14090>.
- 1049 [24] Marco Cirelli et al. “PPPC 4 DM ID: a poor particle physicist cookbook for dark matter  
1050 indirect detection”. In: *Journal of Cosmology and Astroparticle Physics* 2011.03 (Mar.  
1051 2011), p. 051. doi: [10.1088/1475-7516/2011/03/051](https://doi.org/10.1088/1475-7516/2011/03/051). URL: <https://dx.doi.org/10.1088/1475-7516/2011/03/051>.
- 1053 [25] W. B. Atwood et al. “The Large Area Telescope on the Fermi Gamma-Ray Space Telescope  
1054 Mission”. In: *apj* 697.2 (June 2009), pp. 1071–1102. doi: [10.1088/0004-637X/697/2/1071](https://doi.org/10.1088/0004-637X/697/2/1071). arXiv: [0902.1089 \[astro-ph.IM\]](https://arxiv.org/abs/0902.1089).
- 1056 [26] M. Ackermann et al. “Searching for Dark Matter Annihilation from Milky Way Dwarf  
1057 Spheroidal Galaxies with Six Years of Fermi Large Area Telescope Data”. In: *prl* 115.23,  
1058 231301 (Dec. 2015), p. 231301. doi: [10.1103/PhysRevLett.115.231301](https://doi.org/10.1103/PhysRevLett.115.231301). arXiv:  
1059 [1503.02641 \[astro-ph.HE\]](https://arxiv.org/abs/1503.02641).
- 1060 [27] Mattia Di Mauro, Martin Stref, and Francesca Calore. “Investigating the effect of Milky  
1061 Way dwarf spheroidal galaxies extension on dark matter searches with Fermi-LAT data”.  
1062 In: *Phys. Rev. D* 106 (12 Dec. 2022), p. 123032. doi: [10.1103/PhysRevD.106.123032](https://doi.org/10.1103/PhysRevD.106.123032).  
1063 URL: <https://link.aps.org/doi/10.1103/PhysRevD.106.123032>.
- 1064 [28] F. et al. Aharonian. “Observations of the Crab Nebula with H.E.S.S.”. In: *Astron. Astrophys.*  
1065 457 (2006), pp. 899–915. doi: [10.1051/0004-6361:20065351](https://doi.org/10.1051/0004-6361:20065351). arXiv: [astro-ph/0607333](https://arxiv.org/abs/astro-ph/0607333).
- 1067 [29] J. Albert et al. “VHE  $\gamma$ -Ray Observation of the Crab Nebula and its Pulsar with the MAGIC  
1068 Telescope”. In: *The Astrophysical Journal* 674.2 (Feb. 2008), p. 1037. doi: [10.1086/525270](https://doi.org/10.1086/525270). URL: <https://dx.doi.org/10.1086/525270>.
- 1070 [30] N. Park. “Performance of the VERITAS experiment”. In: *Proceedings, 34th International  
1071 Cosmic Ray Conference (ICRC2015): The Hague, The Netherlands, July, 30th July - 6th  
1072 August*. Vol. 34. 2015, p. 771. arXiv: [1508.07070 \[astro-ph.IM\]](https://arxiv.org/abs/1508.07070).
- 1073 [31] A. Abramowski et al. “H.E.S.S. constraints on Dark Matter annihilations towards the Sculptor  
1074 and Carina Dwarf Galaxies”. In: *Astropart. Phys.* 34 (2011), pp. 608–616. doi: [10.1016/j.astropartphys.2010.12.006](https://doi.org/10.1016/j.astropartphys.2010.12.006). arXiv: [1012.5602 \[astro-ph.HE\]](https://arxiv.org/abs/1012.5602).
- 1076 [32] A. Abramowski et al. “Search for dark matter annihilation signatures in H.E.S.S. observations  
1077 of Dwarf Spheroidal Galaxies”. In: *Phys. Rev. D* 90 (2014), p. 112012. doi: [10.1103/PhysRevD.90.112012](https://doi.org/10.1103/PhysRevD.90.112012). arXiv: [1410.2589 \[astro-ph.HE\]](https://arxiv.org/abs/1410.2589).
- 1079 [33] H. Abdalla et al. “Searches for gamma-ray lines and ‘pure WIMP’ spectra from Dark  
1080 Matter annihilations in dwarf galaxies with H.E.S.S”. in: *JCAP* 11 (2018), p. 037. doi:  
1081 [10.1088/1475-7516/2018/11/037](https://doi.org/10.1088/1475-7516/2018/11/037). arXiv: [1810.00995 \[astro-ph.HE\]](https://arxiv.org/abs/1810.00995).

- 1082 [34] J. Aleksić et al. “Optimized dark matter searches in deep observations of Segue 1 with  
1083 MAGIC”. in: *JCAP* 1402 (2014), p. 008. doi: [10.1088/1475-7516/2014/02/008](https://doi.org/10.1088/1475-7516/2014/02/008).  
1084 arXiv: [1312.1535 \[hep-ph\]](https://arxiv.org/abs/1312.1535).
- 1085 [35] V.A. Acciari et al. “Combined searches for dark matter in dwarf spheroidal galaxies observed  
1086 with the MAGIC telescopes, including new data from Coma Berenices and Draco”. In: *Physics of the Dark Universe* (2021), p. 100912. ISSN: 2212-6864. doi: <https://doi.org/10.1016/j.dark.2021.100912>. URL: <https://www.sciencedirect.com/science/article/pii/S2212686421001370>.
- 1089 [36] M. L. Ahnen et al. “Indirect dark matter searches in the dwarf satellite galaxy Ursa Major II  
1090 with the MAGIC Telescopes”. In: *JCAP* 1803.03 (2018), p. 009. doi: [10.1088/1475-7516/2018/03/009](https://doi.org/10.1088/1475-7516/2018/03/009). arXiv: [1712.03095 \[astro-ph.HE\]](https://arxiv.org/abs/1712.03095).
- 1093 [37] S. et al. Archambault. “Dark matter constraints from a joint analysis of dwarf Spheroidal  
1094 galaxy observations with VERITAS”. in: *prd* 95.8 (Apr. 2017). doi: [10.1103/PhysRevD.95.082001](https://doi.org/10.1103/PhysRevD.95.082001). arXiv: [1703.04937 \[astro-ph.HE\]](https://arxiv.org/abs/1703.04937).
- 1096 [38] Louise Oakes et al. “Combined Dark Matter searches towards dwarf spheroidal galaxies with  
1097 Fermi-LAT, HAWC, HESS, MAGIC and VERITAS”. in: *Proceedings of Science*. 2019.
- 1098 [39] Celine Armand et al. on behalf of the Fermi-LAT, HAWC, HESS, MAGIC, VERITAS.  
1099 “Combined Dark Matter searches towards dwarf spheroidal galaxies with Fermi-LAT,  
1100 HAWC, HESS, MAGIC and VERITAS”. in: *Proceedings of Science*. 2021.
- 1101 [40] Daniel Kerszberg et al. on behalf of the Fermi-LAT, HAWC, HESS, MAGIC, and VER-  
1102 TIAS collaborations. “Search for dark matter annihilation with a combined analysis of  
1103 dwarf spheroidal galaxies from Fermi-LAT, HAWC, H.E.S.S., MAGIC and VERITAS”. in:  
1104 *Proceedings of Science*. 2023.
- 1105 [41] A. U. Abeysekara et al. “Observation of the Crab Nebula with the HAWC Gamma-Ray  
1106 Observatory”. In: *The Astrophysical Journal* 843.1 (June 2017), p. 39. doi: [10.3847/1538-4357/aa7555](https://doi.org/10.3847/1538-4357/aa7555). URL: <https://doi.org/10.3847/1538-4357/aa7555>.
- 1108 [42] Giacomo Vianello et al. *The Multi-Mission Maximum Likelihood framework (3ML)*. 2015.  
1109 arXiv: [1507.08343 \[astro-ph.HE\]](https://arxiv.org/abs/1507.08343).
- 1110 [43] Marco Cirelli et al. “PPPC 4 DM ID: a poor particle physicist cookbook for dark matter  
1111 indirect detection”. In: *Journal of Cosmology and Astroparticle Physics* 2011.03 (Mar.  
1112 2011). ISSN: 1475-7516. doi: [10.1088/1475-7516/2011/03/051](https://doi.org/10.1088/1475-7516/2011/03/051). URL: <http://dx.doi.org/10.1088/1475-7516/2011/03/051>.
- 1114 [44] Alex Geringer-Sameth, Savvas M. Koushiappas, and Matthew Walker. “DWARF GALAXY  
1115 ANNIHILATION AND DECAY EMISSION PROFILES FOR DARK MATTER EXPERI-  
1116 MENTS”. in: *The Astrophysical Journal* 801.2 (Mar. 2015), p. 74. ISSN: 1538-4357. doi:

- 1117        10.1088/0004-637X/801/2/74. URL: <http://dx.doi.org/10.1088/0004-637X/80>  
1118        1/2/74.
- 1119 [45] A. Albert et al. “Dark Matter Limits from Dwarf Spheroidal Galaxies with the HAWC  
1120 Gamma-Ray Observatory”. In: *The Astrophysical Journal* 853.2 (Feb. 2018), p. 154. ISSN:  
1121 1538-4357. doi: 10.3847/1538-4357/aaa6d8. URL: <http://dx.doi.org/10.3847/1538-4357/aaa6d8>.
- 1123 [46] V. Bonnivard et al. “Spherical Jeans analysis for dark matter indirect detection in dwarf  
1124 spheroidal galaxies - Impact of physical parameters and triaxiality”. In: *Mon. Not. Roy.  
1125 Astron. Soc.* 446 (2015), pp. 3002–3021. doi: 10.1093/mnras/stu2296. arXiv:  
1126 1407.7822 [astro-ph.HE].
- 1127 [47] Alex Geringer-Sameth and Matthew Koushiappas Savvas M. and Walker. “Dwarf galaxy  
1128 annihilation and decay emission profiles for dark matter experiments”. In: *Astrophys.  
1129 J.* 801.2 (2015), p. 74. doi: 10.1088/0004-637X/801/2/74. arXiv: 1408.0002  
1130 [astro-ph.CO].
- 1131 [48] M. Ackermann et al. “Searching for Dark Matter Annihilation from Milky Way Dwarf  
1132 Spheroidal Galaxies with Six Years of Fermi Large Area Telescope Data”. In: *prl* 115.23,  
1133 231301 (Dec. 2015), p. 231301. doi: 10.1103/PhysRevLett.115.231301. arXiv:  
1134 1503.02641 [astro-ph.HE].
- 1135 [49] A. et al. Albert. “Searching for Dark Matter Annihilation in Recently Discovered Milky Way  
1136 Satellites with Fermi-LAT”. in: *Astrophys. J.* 834.2 (2017), p. 110. doi: 10.3847/1538-4  
1137 357/834/2/110. arXiv: 1611.03184 [astro-ph.HE].
- 1138 [50] Mattia Di Mauro and Martin Wolfgang Winkler. “Multimessenger constraints on the dark  
1139 matter interpretation of the Fermi-LAT Galactic Center excess”. In: *prd* 103.12, 123005  
1140 (June 2021), p. 123005. doi: 10.1103/PhysRevD.103.123005. arXiv: 2101.11027  
1141 [astro-ph.HE].
- 1142 [51] V. Bonnivard et al. “Dark matter annihilation and decay in dwarf spheroidal galaxies: The  
1143 classical and ultrafaint dSphs”. In: *Mon. Not. Roy. Astron. Soc.* 453.1 (2015), pp. 849–867.  
1144 doi: 10.1093/mnras/stv1601. arXiv: 1504.02048 [astro-ph.HE].
- 1145 [52] Gianfranco Bertone, Dan Hooper, and Joseph Silk. “Particle dark matter: evidence, can-  
1146 didates and constraints”. In: *Physics Reports* 405.5-6 (Jan. 2005), pp. 279–390. ISSN:  
1147 0370-1573. doi: 10.1016/j.physrep.2004.08.031. URL: <http://dx.doi.org/10.1016/j.physrep.2004.08.031>.
- 1149 [53] HongSheng Zhao. “Analytical models for galactic nuclei”. In: *Mon. Not. Roy. Astron. Soc.*  
1150 278 (1996), pp. 488–496. doi: 10.1093/mnras/278.2.488. arXiv: astro-ph/9509122  
1151 [astro-ph].

- 1152 [54] H. C. Plummer. “On the Problem of Distribution in Globular Star Clusters: (Plate 8.)”  
1153 In: *Monthly Notices of the Royal Astronomical Society* 71.5 (Mar. 1911), pp. 460–470.  
1154 ISSN: 0035-8711. doi: [10.1093/mnras/71.5.460](https://doi.org/10.1093/mnras/71.5.460). eprint: <https://academic.oup.com/mnras/article-pdf/71/5/460/2937497/mnras71-0460.pdf>. URL:  
1155 <https://doi.org/10.1093/mnras/71.5.460>.
- 1156  
1157 [55] Daniel R. Hunter. “Derivation of the anisotropy profile, constraints on the local velocity  
1158 dispersion, and implications for direct detection”. In: *JCAP* 02 (2014), p. 023. doi:  
1159 [10.1088/1475-7516/2014/02/023](https://doi.org/10.1088/1475-7516/2014/02/023). arXiv: [1311.0256 \[astro-ph.CO\]](https://arxiv.org/abs/1311.0256).
- 1160 [56] Barun Kumar Dhar and Liliya L. R. Williams. “Surface mass density of the Einasto family  
1161 of dark matter haloes: are they Sersic-like?” In: *Mon. Not. Roy. Astron. Soc.* (2010). doi:  
1162 [10.1111/j.1365-2966.2010.16446.x](https://doi.org/10.1111/j.1365-2966.2010.16446.x).
- 1163 [57] M. Baes and E. Van Hese. “Dynamical models with a general anisotropy profile”. In: *Astron. Astrophys.* 471 (2007), p. 419. doi: [10.1051/0004-6361:20077672](https://doi.org/10.1051/0004-6361:20077672). arXiv:  
1164 [0705.4109 \[astro-ph\]](https://arxiv.org/abs/0705.4109).  
1165
- 1166 [58] Matthew G. Walker, Edward W. Olszewski, and Mario Mateo. “Bayesian analysis of re-  
1167 solved stellar spectra: application to MMT/Hectochelle observations of the Draco dwarf  
1168 spheroidal”. In: *mnras* 448.3 (Apr. 2015), pp. 2717–2732. doi: [10.1093/mnras/stv099](https://doi.org/10.1093/mnras/stv099).  
1169 arXiv: [1503.02589 \[astro-ph.GA\]](https://arxiv.org/abs/1503.02589).